

S. Bagheri  
D. S. Henningson

Department of Mechanics and Linné Flow Center,  
Royal Institute of Technology (KTH),  
S-10044 Stockholm, Sweden

J. Høpffner  
Institut de Recherche sur les Phénomènes Hors  
Équilibre (IRPHÉ),  
CNRS-Université d'Aix-Marseille,  
F-13384 Marseille, France

P. J. Schmid  
Laboratoire d'Hydrodynamique (LadHyX),  
CNRS-École Polytechnique,  
F-91128 Palaiseau, France

# Input-Output Analysis and Control Design Applied to a Linear Model of Spatially Developing Flows

*This review presents a framework for the input-output analysis, model reduction, and control design for fluid dynamical systems using examples applied to the linear complex Ginzburg-Landau equation. Major advances in hydrodynamics stability, such as global modes in spatially inhomogeneous systems and transient growth of non-normal systems, are reviewed. Input-output analysis generalizes hydrodynamic stability analysis by considering a finite-time horizon over which energy amplification, driven by a specific input (disturbances/actuator) and measured at a specific output (sensor), is observed. In the control design the loop is closed between the output and the input through a feedback gain. Model reduction approximates the system with a low-order model, making modern control design computationally tractable for systems of large dimensions. Methods from control theory are reviewed and applied to the Ginzburg-Landau equation in a manner that is readily generalized to fluid mechanics problems, thus giving a fluid mechanics audience an accessible introduction to the subject.* [DOI: 10.1115/1.3077635]

## 1 Introduction

Whereas stability theory has long occupied a central role in fluid mechanics research, control theory has only recently been applied to fluid systems. Despite its long history, stability theory has undergone remarkable changes over the past decades. The incorporation of short-term instabilities into a traditionally asymptotic stability concept, the equal treatment of stability and response behavior within the same mathematical framework, and the use of system-theoretical tools to probe the disturbance behavior of fluid systems have reinvigorated hydrodynamic stability theory and developed it into a modern tool of fluid dynamic research. Especially the formulation of the governing equations in state-space form combined with an input-output viewpoint of the perturbation dynamics has brought the two fields of stability and control theory closer together. Whereas stability theory is concerned with all aspects of the open-loop dynamics of the governing equations, control theory connects the output to the input and focuses on the closed-loop characteristics—including optimal design and performance analysis—of the underlying dynamical system. These two closely related disciplines, and the unifying formulation that connects them, are the subjects of this review. Due to the vastness of these two fields, we restrict ourselves to concepts of direct relevance to fluid dynamical systems and to a simple model equation. The Ginzburg-Landau equation, a well-known model equation displaying a great variety of phenomena observed in fluid systems, will be used to demonstrate and exemplify the concepts and techniques from stability, systems, and control theory.

The recognition that short-term instabilities play an important role in fluid dynamical systems can be traced back nearly 2 decades when scientists searched for disturbances that optimize energy amplification over a finite-time span [1–4]. These disturbances did not resemble the most unstable eigenvectors of the system, which led to the development of a theoretical foundation to describe short-term nonmodal phenomena [5–8]. In fact, even if the flow is asymptotically stable, substantial amplification of the input signal (initial condition or external forcing) into an output signal (energy) can occur. By now, the associated theory has matured into an important component for understanding the transi-

tion process from laminar to turbulent fluid motion and has been able to explain a variety of observed fluid structures in transitional and turbulent shear flows [7]. In a further step, an input-output framework has been suggested [9], which brings the analysis of stability characteristics closer to a system theoretic interpretation, with impulse response, frequency response, and transfer functions as the principal tools of investigation.

At the same time, flow control based on control theory has emerged as a new discipline of fluid mechanics ([10–19]). Starting with simple feedback control laws and full-state information control, it has progressed toward more realistic configurations by incorporating the estimation problem and partial-state information control. During the control design process, a strategy is determined that feeds information from the measurements (sensors) back to the input signal (actuators) such that a given control objective is achieved. The accompanying theoretical basis, adapted from control theory [20–23], to determine these strategies has evolved substantially, and flow control has advanced into an independent and active field of fluid dynamics. Comprehensive accounts on recent progress in the rapidly expanding field of flow control can be found in Refs. [24–27].

The input-output framework provides not only a convenient way of analyzing stability and receptivity characteristics [28,29] of fluid systems, but it also represents the natural starting point for control design. Stability and receptivity analysis and control design can thus be accomplished within the same formal setting. This unified analysis shall be exemplified in this review article by investigating the stability and response properties of the Ginzburg-Landau equation and by devising effective control strategies including the evaluation of their efficiency and performance. The Ginzburg-Landau equation has frequently been used as a model for instabilities in fluid systems, see, e.g., Refs. [30,31]. We will use it here with two different sets of parameters: one set to model globally unstable flows (so-called *oscillators*) and another set to describe convectively unstable flows (so-called *noise amplifiers*). The Ginzburg-Landau equation has also been the subject to several flow control studies [32–36].

The review is organized as follows (see also Fig. 1): We start with a summary of stability results for the Ginzburg-Landau equation in Sec. 2 where the results for both asymptotic behavior and transient growth will be presented. In Sec. 3, we investigate the input-output behavior of linear systems in general, and the Ginzburg-Landau equation, in particular. The response to impul-

Manuscript received March 19, 2008; final manuscript received March 26, 2008; published online February 19, 2009. Review conducted by J. N. Reddy.

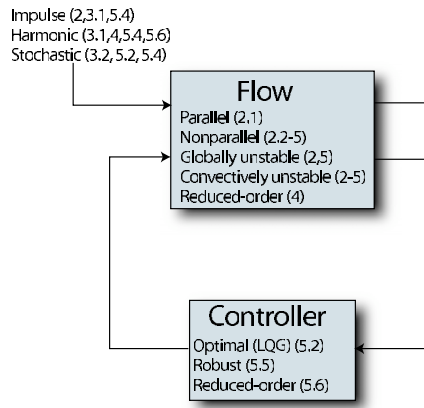


**Fig. 1** Overview of the open-loop and closed-loop analyses performed in this review. The response in terms of the flow state, kinetic energy, and sensor signal to impulse, and harmonic and stochastic inputs of the parallel, nonparallel, convectively unstable, and globally unstable Ginzburg–Landau equation is investigated in Secs. 2 and 3. Model reduction of the system is performed in Sec. 4 followed by optimal (LQG), robust ( $\mathcal{H}_\infty$ ), and reduced-order control design in Sec. 5.

sive, harmonic, and stochastic forcing will be considered, and the concepts of controllability and observability will be introduced. In Sec. 4, we review the projection method of model reduction using global eigenmodes, proper orthogonal decomposition (POD) modes, and balanced truncation. Section 5 deals with the control design for the Ginzburg–Landau equation. We present a detailed derivation of the linear quadratic Gaussian (LQG) control framework, raise the important issue of actuator and sensor placement, and conclude by discussing robust control. Concluding remarks and a summary of the presented material are offered in Sec. 6.

## 2 Asymptotic and Transient Behaviors

**2.1 Parallel Flows: Fundamental Concepts.** Before applying modern techniques of hydrodynamic stability theory [7] to the full Ginzburg–Landau model describing spatially varying flows, we will first introduce and analyze a simpler version of the Ginzburg–Landau equation. By neglecting the spatial dependence of the flow, thus arriving at the parallel (i.e., constant-coefficient) Ginzburg–Landau equation, we will apply concepts of linear stability analysis to describe the growth and decay of disturbances in time and/or space.

The parallel Ginzburg–Landau equation on the infinite interval  $-\infty < x < \infty$  reads

$$\frac{\partial q}{\partial t} = \mathcal{A}q = \left( -\nu \frac{\partial}{\partial x} + \gamma \frac{\partial^2}{\partial x^2} + \mu \right) q \quad (1a)$$

$$q(x, t) < \infty \quad \text{as } x \rightarrow \pm \infty \quad (1b)$$

with initial condition  $q(x, 0) = q_0(x)$  and  $\mathcal{A}$  as the Ginzburg–Landau operator. The solutions  $q(x, t)$  are functions in  $\mathbb{C}$  with the inner-product defined as  $\langle f, g \rangle = \int_{-\infty}^{\infty} f^* g dx$ . We occasionally refer to this norm as the energy norm. The superscript “\*” denotes the complex conjugate. The convective and the dissipative nature of the modeled flow are represented by the complex terms  $\nu = U + 2ic_u$  and  $\gamma = 1 + ic_d$ , respectively. The above equation is of convection-diffusion type with an extra real-valued term  $\mu = \mu_0 - c_u^2$  to model the presence of exponential instabilities. The significance of the complex terms  $c_d$  and  $c_u$  will become clearer when we decompose the system into wavelike solutions.

We first investigate the linear stability of the parallel Ginzburg–Landau equation, i.e., the spatiotemporal evolution of the perturbation  $q(x, t)$  about the basic state  $q_B(x, t) = 0$ . As introduced by Briggs [37], this spatiotemporal evolution of perturbations in fluid flow can be described by three basic types of local behavior: (i) stable, (ii) convectively unstable, and (iii) absolutely unstable. Our model equation, in fact, has by construction the minimum number of required terms to give rise to a successive transition through the three types of instability.

The three types of disturbance behavior can be probed by computing the response to a spatially and temporally localized pulse as this pulse evolves in space and time. Figure 2 demonstrates the three types of responses that may be observed. First, the amplitude may asymptotically decay in time throughout the entire domain (see Fig. 2(a)). In this case, the basic flow is deemed linearly stable. Second, a convectively unstable flow is shown in Fig. 2(b); in this case, the perturbation grows in time but is convected away from the location at which it was generated, so that the response eventually decays to zero at every spatial location. Finally, for an absolutely unstable flow (see Fig. 2(c)) the perturbation is amplified both upstream and downstream of the location; it was generated and thus contaminates the entire spatial domain over time.

The response behavior to a  $\delta$ -function applied at  $(x, t) = (0, 0)$  is equivalent to the Green’s function or impulse response of the complex Ginzburg–Landau equation. We will return to this concept in Sec. 3 of this review. In what follows, we will first exploit the homogeneity in space and time and seek solutions in the wavenumber/frequency (Fourier) space. The dispersion relation linking wavenumber and frequency then fully describes the evolution of wavelike (and by superposition) nonwavelike solutions. Criteria for stability or instability of the solutions, as well as the type of instability, follow easily from the dispersion relation.

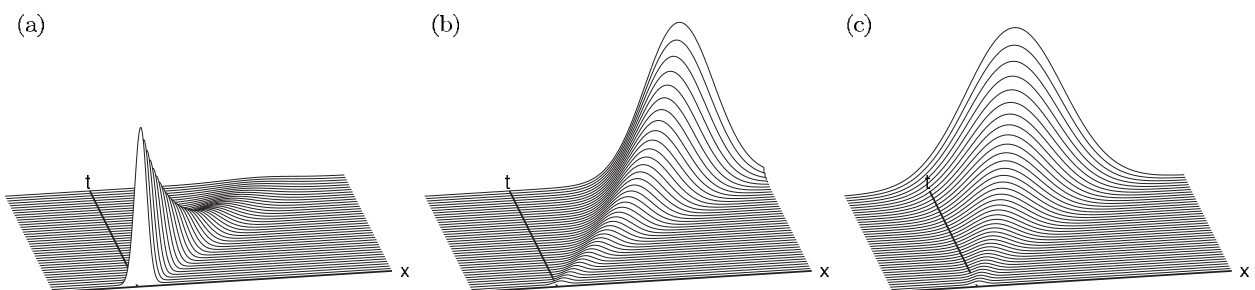


**Fig. 2** Local stability concepts based on the linear response of the parallel Ginzburg–Landau equation to a temporally and spatially localized pulse at  $t=0$  and  $x=0$ , displayed in the  $x$ - $t$ -plane. (a) Stable configuration  $\mu_0 \leq 0$ : The solution at  $t=t_1 > 0$  is damped everywhere. (b) Convectively unstable configuration  $0 < \mu_0 < \mu_1$ : The solution at  $t=t_1$  is amplified but is zero along the ray  $x/t=0$ . (c) Absolutely unstable configuration  $\mu_1 \leq \mu_0$ : The state is amplified at  $t=t_1$  and nonzero along the ray  $x/t=0$ .

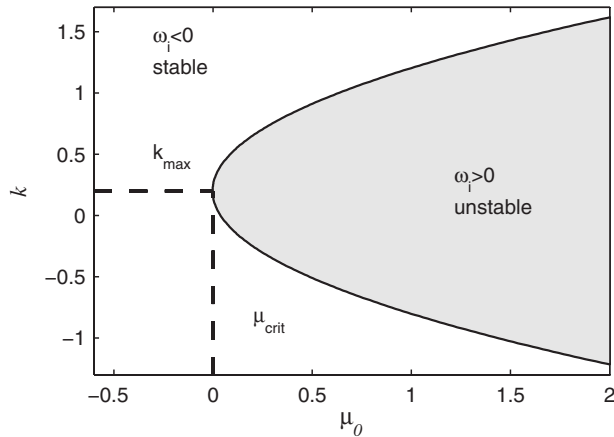


**Fig. 3 The neutral stability curve for the parallel Ginzburg–Landau equation (with  $c_u=0.2$ ) in the  $(\mu_0, k)$ -plane**

We express the solutions  $q(x, t)$  as a superposition of normal modes  $\tilde{q}(k, \omega)\exp(ikx - i\omega t)$  with wavenumber  $k$ , frequency  $\omega$ , and (complex) amplitude  $\tilde{q}$ . The imaginary part of  $k$  and  $\omega$  determines the stability of the associated solution, whereas the real part describes the oscillatory behavior in  $x$  and  $t$ , respectively. Introducing this normal mode decomposition into Eq. (1) results in the dispersion relation,  $D(k, \omega; \mu_0)=0$ , which takes the form

$$\omega = U k + c_d k^2 + i(\mu_0 - (k - c_u)^2) \quad (2)$$

Within the temporal framework, an initial periodic perturbation with *real* wavenumber  $k$  grows exponentially in time when  $\mu_0$  in Eq. (2) exceeds  $(k - c_u)^2$ , i.e., when exponential growth exceeds diffusion. In this case,  $\omega_i(k) > 0$  and the associated normal mode  $\tilde{q}$  exhibit exponential temporal growth. Furthermore, we observe a finite interval  $k \in [c_u - \sqrt{\mu_0}, c_u + \sqrt{\mu_0}]$  of unstable spatial wavenumbers. A simple criterion for linear stability of the flow can be deduced by considering the growth rate  $\omega_i = \omega_{i,\max}$  of the most unstable wave  $k = k_{\max}$  in this interval. For the dispersion relation (2), we observe that  $k_{\max} = c_u$  and the corresponding growth rate is  $\omega_{i,\max} = \mu_0$ . Thus, the condition for a local linear instability becomes

$$\mu_0 \leq 0 \quad \text{locally stable} \quad (3a)$$

$$\mu_0 > 0 \quad \text{locally unstable} \quad (3b)$$

In Fig. 3, the neutral curve, defined by  $\omega_{i,\max}=0$ , is displayed as a function of  $\mu_0$  and  $k$ . We see that the range of unstable wavenumbers increases as  $\mu_0$  increases.

To further investigate the two types of locally unstable configurations—convectively unstable and absolutely unstable—it is instructive to consider perturbations that consist of a superposition of normal modes near  $k=c_u$ , which form a traveling wavepacket. From the dispersion relation (2), we conclude that individual wave components of this wavepacket travel at the phase velocity

$$\omega_r/k = U + c_d k \quad (4)$$

whereas the wavepacket itself, and therefore the perturbation, travels at the group velocity

$$U_{\max} = \frac{\partial \omega}{\partial k} = U + 2c_d c_u \quad (5)$$

In general, the group velocity is complex but carries a physical meaning when it is real, which is always the case for the most unstable wavenumber  $c_u$ .

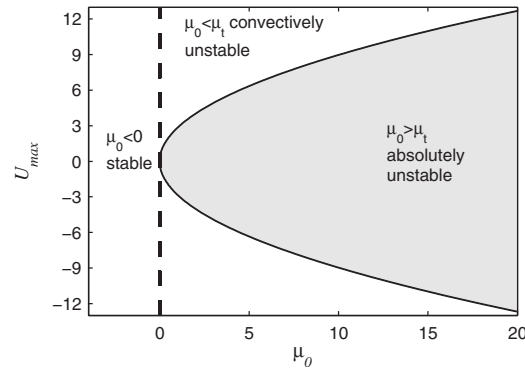


**Fig. 4 The neutral absolute stability curve for the parallel Ginzburg–Landau equation (with  $\gamma=1-i$ ) in the  $(\mu_0, U_{\max})$ -plane**

The disturbance behavior in the unstable region depends on the competition between convection and instability. For the Ginzburg–Landau equation, we find that the flow is convectively unstable if  $U_{\max} > 2\sqrt{\mu_0|\gamma|}$ , i.e., when the group velocity exceeds the exponential instability of the unstable region (for constant diffusion). This means that, for convection-dominated flows, perturbations grow as they enter the unstable domain but are quickly convected downstream, beyond the unstable region where they decay, and the basic state relaxes back to its original state (see Fig. 2(b)). However, when  $\mu_0$  exceeds the critical value of

$$\mu_t = \frac{U_{\max}^2}{4|\gamma|^2} \quad (6)$$

there exists an unstable wavelength with zero group velocity. As the perturbation is amplified in the unstable domain, it will gradually contaminate the entire physical domain and render the flow absolutely unstable. In Fig. 4, the neutral curve, defined by  $\mu_t = 0$ , is displayed as a function  $\mu_0$  and  $U_{\max}$ . The critical value  $\mu_t$  is obtained by considering a wavepacket with a zero group velocity  $\partial\omega/\partial k=0$  (see Ref. [38] for an exact derivation). The associated growth rate  $\omega_i = \omega_{i,0}$  is the absolute growth rate. Unlike for our case, the absolute frequency  $\omega_0$  for realistic flow configurations can seldom be found in analytic form. Instead, one has to resort to Briggs' method [37] (see also Ref. [38]), which amounts to locating pinch points in the complex  $k$ -plane. In addition to the criterion of zero group velocity, one must ensure that the two spatial branches  $k^+(\omega)$  and  $k^-(\omega)$  (for real  $\omega$ ) in Eq. (2) originate from the upper and lower halves of the complex  $k$ -plane.

**2.2 Spatially Developing Flows: A Global Approach.** Despite the limitations of a parallel flow assumption, the above results carry over to weakly nonparallel flows as described in Refs. [31,39–41]. Within a Wentzel–Kramers–Brillouin–Jeffreys (WKBJ) approximation, one can draw conclusions about the global stability behavior from investigating the dispersion relation locally. Many realistic flows, however, are strongly nonparallel, which requires us to resort to a global stability analysis. In this section, we will adopt this global point of view to investigate the stability properties of a simple model flow, which depends on the flow direction  $x$ . We will see that a rich disturbance behavior is uncovered, which has its roots in the non-normality of the underlying evolution operator [42–44]. As a first step, one solves a global eigenvalue problem. Assuming completeness, any perturbation can then be decomposed into the global eigenfunctions of the governing operator. If there exists an unstable global mode, it is amplified until it saturates due to the nonlinearity and may lead to self-sustained oscillations in the flow (Fig. 5). The short-time, or transient, behavior can also be captured by global modes [46,47], if one considers a superposition of them. For non-normal stability operator with corresponding nonorthogonal global

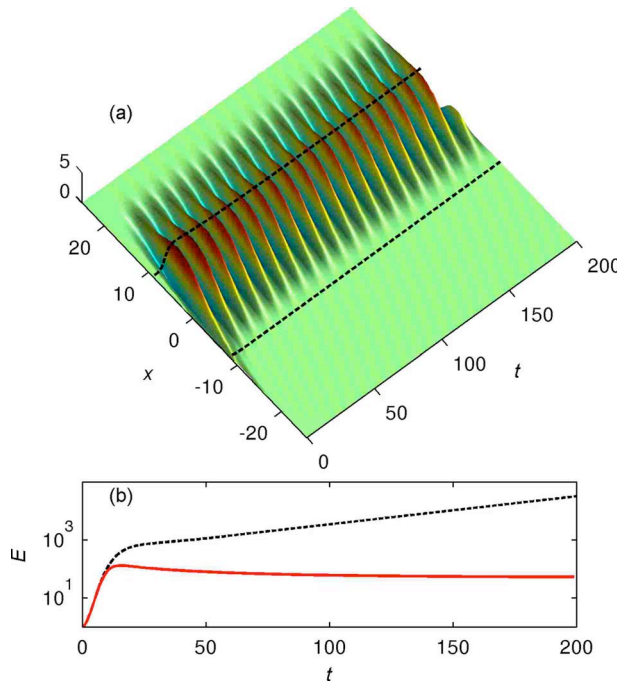


**Fig. 5** (a) The spatiotemporal evolution of a disturbance in a globally unstable flow. The disturbance grows exponentially until the cubic nonlinear term  $-|q|^2 q$  (see Refs. [30,45] for details of the nonlinear Ginzburg–Landau equation) causes the disturbance to saturate and oscillate. (b) The energy that corresponds to the evolution in (a) is shown in red, and the linear exponential growth for the linear Ginzburg–Landau equation is shown in dashed black.

modes, a superposition of decaying global modes can result in a large transient amplification of perturbation energy (Fig. 6). As demonstrated by Cossu and Chomaz [46], this transient behavior often corresponds to a localized convective instability when using a local approach.

The linear complex Ginzburg–Landau equation serves as a simple model for capturing both the short-time and long-time evolution of small perturbations  $q(x,t)$  in spatially developing flows. We will use this model equation to illustrate fundamental concepts of linear global stability analysis. If the parameter  $\mu$ , responsible for the local instability in Eq. (1), is now taken as a function of  $x$ , the Ginzburg–Landau equation becomes a variable-coefficient partial differential equation modeling nonparallel flows [48]. The Ginzburg–Landau equation with  $\mu$  as a linear function in  $x$  can be used to mimic flows on the interval  $[0, \infty)$ , as shown in Ref. [49]. We will adopt the commonly used quadratic function [46,48]

$$\mu(x) = (\mu_0 - c_u^2) + \mu_2 \frac{x^2}{2}, \quad \mu_2 < 0 \quad (7)$$

The flow is now susceptible to instabilities only when  $\mu(x) > 0$ , which defines a confined unstable region in the  $x$ -direction given by  $-\sqrt{-2(\mu_0 - c_u^2)/\mu_2} < x < \sqrt{-2(\mu_0 - c_u^2)/\mu_2}$ . The upstream and downstream edges of the unstable domain are referred to as branches I and II, respectively, and are indicated by the two black dashed lines in Figs. 5 and 6. The extent of this region depends on the parameter  $\mu_2$ , which can be interpreted as the degree of nonparallelism of the flow. The operator  $\mathcal{A}$  in Eq. (1) with  $q(x,t)$  bounded for  $x = \pm \infty$  is non-normal if both the term involving  $\mu_2$  and the convection term  $\nu$  are nonzero. As demonstrated in Refs. [30,46], the smaller  $\mu_2$  and/or the larger  $\nu$ , the stronger the nonnormality of the operator  $\mathcal{A}$ . The parameter  $\mu_2$  thus plays a dual role: For large values of  $\mu_2$ , the system is strongly nonparallel but

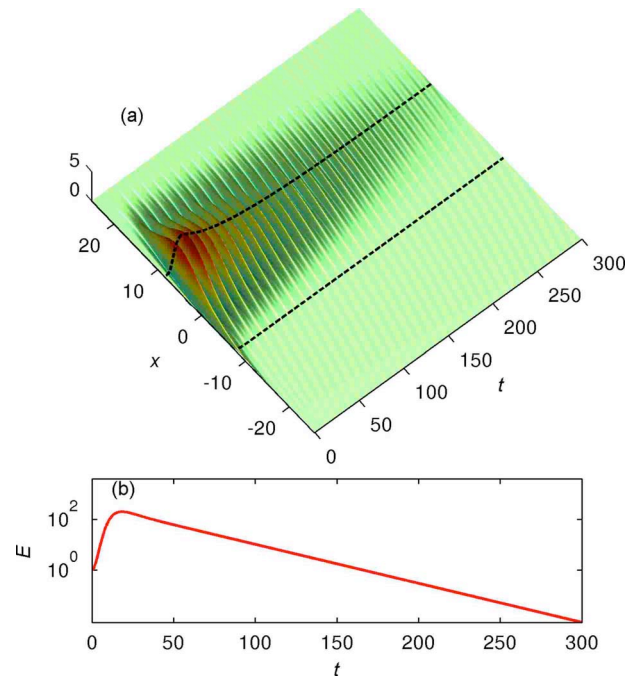


**Fig. 6** (a) Linear transient growth of a perturbation in space and time: An optimal initial perturbation grows as it enters the unstable domain at branch I at  $x = -8.2$  until it reaches branch II at  $x = 8.2$ . The two dashed lines depict branches I and II. (b) The corresponding optimal energy growth of the convectively unstable flow in (a).

weakly non-normal, while for very small values of  $\mu_2$  the system represents weakly nonparallel but strongly non-normal flow. For the latter case, a local analysis may be more appropriate as the resulting global eigensystem is rather ill conditioned [30,44].

A global mode of the Ginzburg–Landau equation is defined as

$$q(x,t) = \phi(x)\exp(\lambda t) \quad (8)$$

and is a solution to the eigenvalue problem

$$\lambda \phi(x) = \mathcal{A} \phi(x) \quad \phi(x) < \infty \quad \text{as } x \rightarrow \pm \infty \quad (9)$$

where  $\mathcal{A}$  is the operator defined in Eq. (1). The flow is globally unstable when the real part of any eigenvalue  $\lambda$  is positive, which results in self-excited linear oscillations in the flow of a frequency given by the imaginary part of  $\lambda$ . For the case  $\mu_2 \neq 0$ , the eigenvalue problem (9) for the Ginzburg–Landau equation (1) can be solved analytically [50]. One obtains

$$\lambda_n = (\mu_0 - c_u^2) - (\nu^2/4\gamma) - (n + 1/2)h \quad (10a)$$

$$\phi_n(x) = \exp\{(\nu/2\gamma)x - \chi^2 x^2/2\} H_n(\chi x) \quad (10b)$$

with  $h = \sqrt{-2\mu_2\gamma}$ ,  $n = 0, 1, \dots$ , and  $H_n$  as the  $n$ th Hermite polynomial, scaled with  $\chi = (-\mu_2/2\gamma)^{1/4}$ . Global instability is determined by the sign of the first eigenvalue ( $n=0$ ), which yields the criterion for global instability as  $\mu_0 > \mu_c$ , where

$$\mu_c = \mu_t + \frac{|h|}{2} \cos\left(\frac{\text{Arg } \gamma}{2}\right) \quad (11)$$

and  $\mu_t$  is the threshold value for absolute instability (6). The term  $\text{Arg}$  denotes the phase angle of  $\gamma$ . We therefore conclude from Eq. (11) that the threshold for a global instability is higher than the one for an absolute instability. Formulated in another way, an absolute instability is a necessary condition for a global instability.

The short-time behavior of a disturbance cannot be predicted by studying individual eigenmodes. Instead, a more detailed analysis

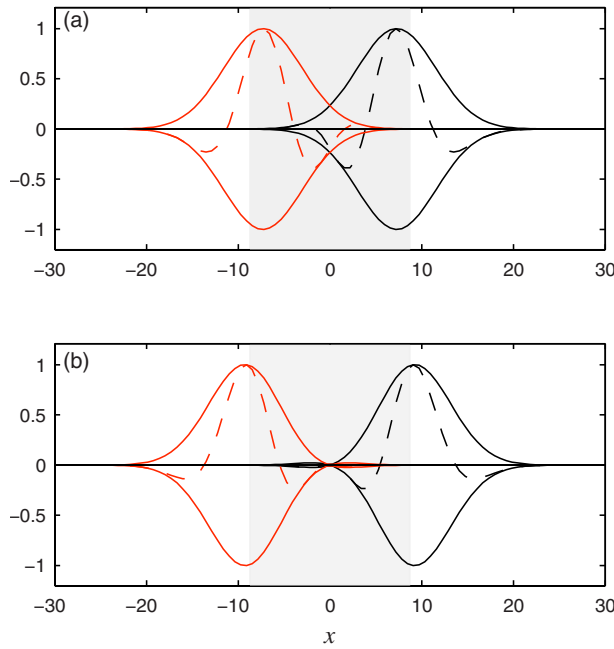


**Fig. 7** The first (a) and second (b) global (black lines) and adjoint eigenmodes (red lines) of the Ginzburg–Landau equation with the absolute value shown in solid and the real part in dashed. The gray area marks the region of instability.

of the properties of the stability operator  $\mathcal{A}$  is necessary. When  $\mu_2 \neq 0$  and  $\nu \neq 0$ , the Ginzburg–Landau operator  $\mathcal{A}$  is non-self-adjoint [42], i.e.,  $\langle q_1, \mathcal{A}q_2 \rangle \neq \langle \mathcal{A}q_1, q_2 \rangle$ . As a consequence, the global modes are nonorthogonal  $\langle \phi_n, \phi_m \rangle \neq \delta_{nm}$  and although they may form a complete basis, they are nearly collinear and their superposition may lead to large transient growth (Fig. 6(b)). We will study this issue in more detail by considering an expansion in global modes. To this end, we find the adjoint global modes as

$$\psi_n(x) = \exp\left(-\nu^*/\gamma^*\right)x \phi_n^*(x) \quad (12)$$

which satisfy the adjoint eigenvalue problem

$$\lambda_n^* \psi_n(x) = \mathcal{A}^* \psi_n(x) \quad (13)$$

where

$$\mathcal{A}^* = \nu^* \frac{\partial}{\partial x} + \gamma^* \frac{\partial^2}{\partial x^2} + \mu^*(x) \quad (14)$$

with boundary condition  $\psi_n(x) < \infty$  as  $x \rightarrow \pm \infty$ . The superscript “\*” denotes the complex conjugate. The adjoint global modes  $\psi_n$  are bi-orthogonal to the global modes (9) according to

$$\langle \psi_n, \phi_m \rangle = N_{nm} \delta_{n,m} \quad (15)$$

with  $N_{nm}$  as a normalization factor that we choose such that  $\|\phi_n\| = \|\psi_n\| = 1$ . The adjoint mode (12) distinguishes itself from its direct counterpart (10b) mainly by the sign of the basic flow convection term  $\nu$ . This manifests itself by a characteristic separation of the direct and adjoint global modes in space. In Figs 7(a) and 7(b), the two first direct and adjoint global modes of the Ginzburg–Landau equation are shown where the separation in  $x$  is seen to increase for higher modes, until the support of the direct and adjoint modes is nearly disjoint. Consequently,  $N_{nm} = \langle \phi_n, \psi_n \rangle$  becomes increasingly small, a phenomenon we shall investigate further in what follows.

We continue by stating that a sequence of global modes  $\{\phi_n\}_{n=0}^\infty$  forms a basis if any solution of the Ginzburg–Landau equation has a norm-convergent expansion

**Table 1** Parameters  $\{\mu_0, \mu_2\}$  and  $\{\nu, \gamma\}$  of the Ginzburg–Landau equation given in Eqs. (1) and (7). The critical values for global and absolute stabilities are  $\mu_c = 0.3977$  and  $\mu_t = 0.32$ , respectively. External disturbances ( $B_1$ ), sensor ( $C_2$ ), and actuator ( $B_2$ ) are Gaussian functions (see Eqs. (A4)) with mean given by  $x_w$ ,  $x_s$ , and  $x_u$ , respectively, and a width of  $s = 0.4$ . Design parameters  $\{R, W, G, \gamma_0\}$  for the LQG and  $\mathcal{H}_\infty$ -compensators are the control penalty ( $R$ ), the covariance of the disturbance ( $W$ ) and sensor noise ( $G$ ), and a bound on the  $\infty$ -norm, ( $\gamma_0$ ).

	Subcritical	Supercritical
$\{\mu_0, \mu_2\}$	{0.38, -0.01}	{0.41, -0.01}
$\{\nu, \gamma\}$	{2+0.2i, 1-i}	{2+0.2i, 1-i}
$\{x_I, x_{II}\}$	{±8.2}	{±8.2}
$\{x_w, x_s, x_u, s\}$	{-11, 0, -3, 0.4}	{-11, 9, -9, 0.1}
$\{R, W, G, \gamma_0\}$	{1, 1, 0.1/1, 0.9}	{1, 0, 1, 9}

$$q(x, t) = \sum_{n=0}^{\infty} \kappa_n \phi_n(x) \exp(\lambda_n t) \quad (16)$$

where the expansion coefficients  $\kappa_n$  are obtained using the adjoint global modes and the initial condition  $q_0$  according to

$$\kappa_n = \frac{\langle q_0, \psi_n \rangle}{\langle \phi_n, \psi_n \rangle} \quad (17)$$

The denominator of the above expression, i.e.,  $N_{nn}$ , becomes very small when the direct and adjoint global modes have nearly disjoint spatial support. In this case, the expansion coefficients (17) of  $q$  become large. Although the amplitude of all stable global modes decreases monotonically in time, their superposition produces a wavepacket that transiently grows in time as it propagates in space.

Although it is possible [10,47,51,52], in practice the short-time amplification of disturbances is rarely computed using global modes. Instead one computes the norm of the exponential matrix [53],  $\|e^{\mathcal{A}t}\|$ , as we shall demonstrate next.

**2.3 Optimal Energy Growth and Resolvent Norms.** For sufficiently large transient amplifications, nonlinear effects can no longer be neglected, and, in real flows, more complex instabilities or transition to turbulence are often triggered. For this reason, it seems important to investigate the most dangerous initial condition that results in a maximum energy amplification over a specified time interval [2–5,55,56].

For simplicity, we will formulate and present results using the discrete Ginzburg–Landau operator  $\mathcal{A}$ . See Appendix for details of the numerical approximation of the operator  $\mathcal{A}$ . The continuous approach can be found in Ref [44]. The values of the Ginzburg–Landau parameters used in the computations that follow can be found in Table 1.

The discrete energy norm given by Eq. (A3) can, after a Cholesky decomposition of the energy weight matrix  $M = F^H F$ , be related to the standard Euclidean norm of a disturbance by

$$E(t) = \|q\|_M^2 = \|Fq\|_2^2 \quad (18)$$

We can now define the maximum transient growth of the perturbation energy at time  $t$  as

$$E_{\max}(t) = \max_{\|q_0\| > 0} \frac{\|q(t)\|_M^2}{\|q_0\|_M^2} = \max_{\|q_0\| > 0} \frac{\|Fe^{At}q_0\|_2^2}{\|Fq_0\|_2^2} = \|Fe^{At}F^{-1}\|_2^2 = \sigma_1^2 \quad (19)$$

where  $\sigma_1$  is determined from a singular value decomposition

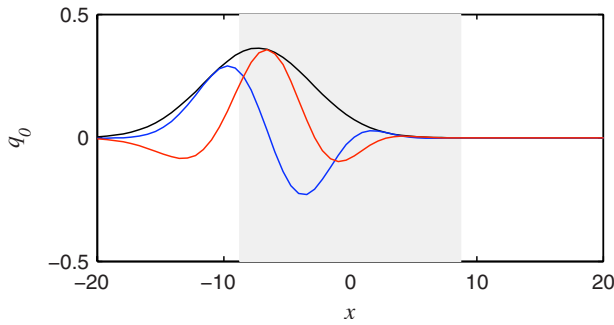


**Fig. 8** Shape of an optimal disturbance with the absolute value shown in black, the real and imaginary parts shown in blue and red, respectively. The gray region marks the unstable region, where disturbances grow exponentially. The maximum value of the optimal disturbance is located close to branch I.

$$Fe^{At}F^{-1} = U\Sigma V^H, \quad \Sigma = \text{diag}\{\sigma_1, \dots, \sigma_n\} \quad (20)$$

The above expression contains an optimization over all possible initial conditions, and the peak value of  $\sigma_1^2(t)$  is the maximum energy amplification over time. Optimal initial disturbances can be calculated according to  $q_0 = F^{-1}V_1$  where  $V_1$  is the right principal singular vector of the SVD in Eq. (20). The maximum growth and the corresponding optimal disturbance can also be obtained from power iterations [7,54].

The optimal initial disturbance of the Ginzburg–Landau equation shown in Fig. 8 is located at the upstream boundary of the unstable domain. As the time evolves, it traverses the unstable domain (gray region), where it can exhibit either decay, transient growth, or asymptotic exponential growth, as illustrated in Fig. 9, depending on the value of bifurcation parameter  $\mu_0$  (i.e., the Reynolds number for Navier–Stokes equations). The optimal energy growth curves shown in Fig. 9 correspond to stable (S), convectively unstable (CU), and globally unstable (GU) flow configurations. Note that, for both S and CU configurations, all global modes are stable. However, only for the latter case do we have  $\mu_0 > 0$  yielding a locally convectively unstable spatial region. Consequently, a transient energy growth of two orders of magnitude can be observed before asymptotic decay sets in Ref. [46].

To conclude this section, we investigate the effect on global modes and on the global spectrum as the operator  $\mathcal{A}$  is discretized.

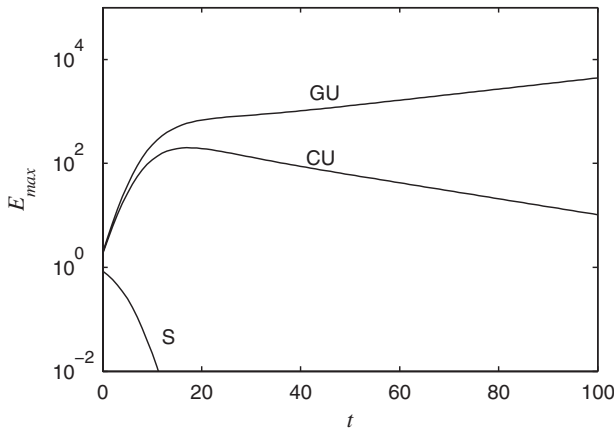


**Fig. 9** Optimal energy growth,  $E_{\max}$ , as a function of time. S configuration  $\mu_0 < 0$ : The perturbation energy decays exponentially for all time. CU configuration  $0 < \mu_0 < \mu_c$ : The perturbation energy is amplified initially but decays to zero asymptotically. GU configuration  $\mu_c < \mu_0$ : The perturbation energy grows exponentially asymptotically. The values of the parameters used in the computations are listed in Table 1.

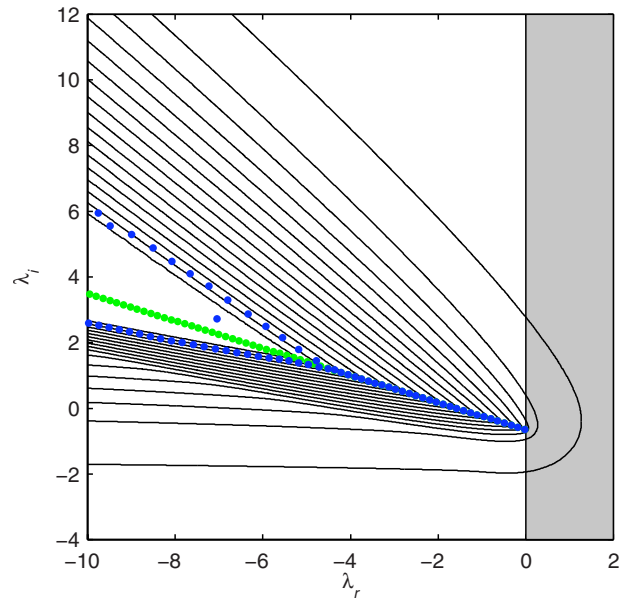


**Fig. 10** Global spectrum of the subcritical Ginzburg–Landau equation (see Table 1), where all the eigenvalues (blue dots) are in the stable half-plane. The unstable domain is in gray and the exact global spectrum is indicated in green. The numerically computed global eigenvalues (blue dots) exhibit a characteristic split, aligning with the resolvent contour that approximately represents machine precision. The resolvent norm contours range from  $10^{-1}$  to  $10^{15}$ .

The spectrum of  $\mathcal{A}$  is displayed in Fig. 10 by the green symbols using the analytical expression (10a). The spectrum of the discretized Ginzburg–Landau operator  $A$  is shown by the blue symbols. A characteristic split of the eigenvalue branch is observed, which is rather common in finite-precision stability computations of strongly non-normal flows. The reason for this split is the insufficient resolution to accurately capture the increasingly oscillatory behavior of the associated eigenfunctions. These observations are closely related to the notion of pseudospectra [44].

It is misleading to assume that if  $A\phi \approx s\phi$ , then  $s$  is close the spectrum of  $A$ . If  $s$  is taken as an approximate eigenvalue in the sense that  $\|A\phi - s\phi\|_M < \epsilon\|\phi\|_M$ , we can conclude that, for normal systems,  $\epsilon$  can be as chosen as small as one wishes. For non-normal systems, however, the minimum value of  $\epsilon$  can become very large. This observation suggests the definition of the pseudospectrum of  $A$  as the sets in the complex plane such that

$$\{s \in \mathbb{C} : \|R(s)\|_M = \|(sI - A)^{-1}\|_M > \epsilon^{-1}\} \quad (21)$$

The pseudospectrum of  $A$  (shown in Fig. 10) is visualized as a contour plot of the norm of the resolvent

$$\|R(s)\|_M = \|FR(s)F^{-1}\|_2 = \sigma_1(s) \quad (22)$$

where  $\sigma_1(s)$  is the largest singular value of  $FR(s)F^{-1}$ . It is then straightforward to conclude that the eigenvalues of the discretized Ginzburg–Landau operator  $A$  are, in fact,  $\epsilon$ -pseudoeigenvalues for  $\epsilon$  equal to machine precision and thus align with the  $10^{15}$  contour of the resolvent norm in Fig. 10. For an alternative approach to characterize the system sensitivity, see Ref. [57].

The resolvent contours moreover give an indication of the existence of non-normal effects, since the amount by which the contours protrude into the unstable half-plane can be used to estimate the maximum transient growth of energy [6,44]. We will return to this concept and use the resolvent norm from an input-output viewpoint in Sec. 3.1, where we generalize the resolvent to transfer functions—one of the most central concepts in the design of control strategies.

**2.4 Stability of Supercritical and Subcritical Flows.** Based on the global and local stability concepts introduced in Secs. 2.1–2.3, we are now in a position to define two fundamentally different scenarios that model the behavior of disturbances in a large number of flows.

The first model is known as the supercritical case, in which any flow disturbance will grow exponentially until it saturates due to nonlinearities, as shown in Fig. 5. A global analysis shows at least one unstable eigenmode of  $\mathcal{A}$ , yielding a globally unstable flow. This type of scenario prevails when the bifurcation parameter  $\mu_0$  of the Ginzburg–Landau equation is larger than the threshold  $\mu_c$ . A local analysis confirms an absolutely unstable region since  $\mu_c > \mu_t$  in Eq. (11) with  $\mu_t$  as the threshold for a local absolute instability (given by Eq. (6)). For more details on how the absolutely unstable region acts as a “wavemaker” that sheds waves in the downstream and upstream direction, see Ref. [30]. Here, we will simply state the fact that linear local stability theory can predict the occurrence of unstable global modes and provide an estimate of the frequency at which these modes oscillate. The Karman vortex street behind a circular cylinder is a generic supercritical flow configuration, and a global and local analysis of the cylinder wake can be found in Refs. [58,59]. It was first shown [60] that the transition in a wake behind a cylinder close to the critical Reynolds number is described by the Landau equation, i.e., the nonlinear Ginzburg–Landau equation without diffusion term. Since then, the Ginzburg–Landau equation (often in its nonlinear form) has been used extensively to model cylinder wakes, see Refs. [32,34,61–63]. Other globally unstable flow examples that have been investigated as to their self-sustained oscillatory behavior are, among others, hot jets [64,65] and a separated boundary layer flow over a bump [66].

The second model is known as the subcritical case and describes the behavior of disturbances in convectively unstable flows (Fig. 6). As a result of the non-normality of  $\mathcal{A}$ , a global analysis reveals the presence of transient energy growth (Fig. 6(b)), which cannot be captured by considering individual eigenmodes of the operator  $\mathcal{A}$ . Instead, one has to consider a superposition of global modes or the norm of the exponential matrix to accurately describe this short-term phenomenon. Transient growth is observed for the Ginzburg–Landau equation when  $0 < \mu_0 < \mu_c$ . A local analysis shows that this corresponds to a region where the flow is convectively unstable. The wavepacket in Fig. 6 travels with a group velocity ( $U_{\max}$ ) composed of a dominant wave ( $c_u$ ), which is associated with the local dispersion relation (2) analyzed in Sec. 2.1. Prototypical convectively unstable flow configurations contain, among others, the boundary layer on a flat plate [51,52], homogeneous jets, and mixing layers [67].

The Ginzburg–Landau parameters  $\{\nu, \mu_0, \mu_2, \gamma\}$  for modeling the linear stability of a subcritical or supercritical flow are listed in Table 1. The critical value, which delineates the two scenarios, is  $\mu_c=0.4$ .

### 3 Input-Output Behavior

Input-output analysis is a type of analysis of linear systems that is commonplace in systems theory [68]. It is concerned with the general response behavior to various excitations of the linear system. In its generality, it goes beyond the concept of classical stability theory commonly practiced in fluid dynamics, as it is not only concerned with issues of stability (i.e., the response to various initial conditions) but also with the short-term dynamics, the response to external (deterministic or stochastic) excitations, and the influence of uncertainties in the underlying system [9]. As such, it is thought of as an extension of stability analysis and helps reveal a more complete picture of the behavior of disturbances governed by the linear system.

The temporal response of the Ginzburg–Landau equation to initial conditions (both short-term transient and long-term asymptotic) has been considered in Sec. 2. In this section, we recast the Ginzburg–Landau model into an input-output frame-

work. The analysis is applied to the convectively unstable case only, since these types of flows are sensitive to forcing and act as noise amplifiers [38]. Globally unstable flows behave as *flow oscillators* with a well-defined frequency that is rather insensitive to external forcing.

This framework will build the foundation for the subsequent design of control schemes, since it allows the quantitative description of the open-loop dynamics, i.e., the response to, for example, excitation in the freestream or to blowing/suction at the wall. We will denote the input sources by  $u(t)$  and the measured outputs by  $y(t)$ . In many realistic flow cases, the output  $y(t)$  will only be a subset of the state variable  $q(t)$ . For example, only shear or pressure measurements at the wall (or another specific location) will be available.

The common format for an input-output analysis is given by the state-space formulation

$$\dot{q}(t) = Aq(t) + Bu(t) \quad (23a)$$

$$y(t) = Cq(t) \quad (23b)$$

$$q(0) = q_0 \quad (23c)$$

where  $A$  represents the discrete Ginzburg–Landau operator, the matrices  $B$  and  $C$  govern the type and location of the inputs  $u(t)$  and outputs  $y(t)$ , respectively, and  $q_0$  stands for the initial condition. For the state-space formulation of the linearized incompressible Navier–Stokes equations see Refs. [9,69].

The continuous equations are discretized in space using a spectral Hermite collocation method described in the Appendix. The inputs  $B=\{B_1, \dots, B_p\}$  and outputs  $C=\{C_1, \dots, C_r\}^H$  have spatial distributions of the form of Gaussian functions given by Eq. (A4). In what follows, we will formulate and present results based on matrices and the *discrete* Ginzburg–Landau operator  $A$ .

The corresponding adjoint state-space equations of Eq. (23), describing the evolution of adjoint state variable  $r(t)$ , can be written as (see also Ref. [70])

$$\dot{r}(t) = A^+r(t) + C^+v(t) \quad (24a)$$

$$z(t) = B^+r(t) \quad (24b)$$

$$r(0) = r_0 \quad (24c)$$

The discrete adjoint matrices are not simply the complex conjugate transpose (in other words,  $(A^+, B^+, C^+) \neq (A^H, B^H, C^H)$ ), unless the inner product used to derive the adjoint operator (13) has an associated weight  $M$ , which is unity. For the more general case,  $M \neq I$ , we have

$$A^+ = M^{-1}A^HM \quad (25a)$$

$$B^+ = B^HM \quad (25b)$$

$$C^+ = M^{-1}C^H \quad (25c)$$

where  $M$  is a positive definite and Hermitian weight matrix. In this work,  $M$  is chosen such that the inner product produces the energy of the state variable (see Appendix).

The system of Eq. (23) has the formal solution

$$y(t) = Ce^{At}q_0 + C \int_0^t e^{A(t-\tau)}Bu(\tau)d\tau \quad (26)$$

where we identify the first part of the right-hand side with the homogeneous solution and the second part with the particular solution stemming from the forcing term  $Bu$ . Having covered the homogeneous solution (for  $C=I$ ) in detail in Sec. 2, we now turn our attention to the particular solution. Setting  $q_0=0$  leaves us with the input-output relation

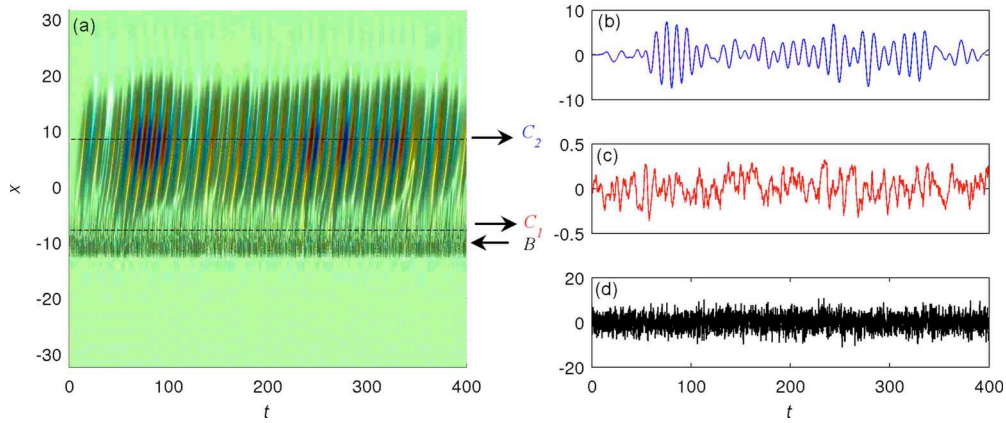


**Fig. 11 Example of the input-output behavior of the Ginzburg–Landau equation with one input and two outputs.** In (a) the evolution in space and time of the state when forced by random noise is shown. The region between the dashed lines is convectively unstable. The locations of the forcing  $B$  ( $x=-11$ ), the first output  $C_1$  (at branch I), and the second output  $C_2$  (at branch II) are marked by arrows. In (b) and (c), the output signals  $y_1=C_1q$  and  $y_2=C_2q$  are shown, and in (d) the input signal  $u$  is shown. Note that in (c) the amplitude of the output signal  $y_1$  is less than 1, but further downstream in (b), the second output signal  $y_2$  has an amplitude close to 10. This illustrates the amplifying behavior of the system.

$$y(t) = C \int_0^t e^{A(t-\tau)} Bu(\tau) d\tau \quad (27)$$

from which we will develop tools to capture and characterize aspects of the transfer behavior of an input signal  $u(t)$  as it is passes through the linear system given by  $A$ .

Before analyzing the above input-output relation in all generality, a first simple numerical experiment shall demonstrate the response behavior of the convectively unstable Ginzburg–Landau equation (see Fig. 11). As an input signal  $u(t)$ , we choose white noise—drawn from a normal distribution with zero mean and unit variance—introduced at a location just upstream of the unstable region; the corresponding response  $y(t)=Cq(t)$  is extracted at the two boundaries of the unstable domain, i.e., at branches I and II. The first observation confirms the amplification of the signal as it traverses the unstable domain and the emergence of a distinct frequency from the noisy input. The system, thus, seems to act as both a noise amplifier [31] and a filter. These two characteristics will be analyzed in more detail below.

**3.1 Impulsive and Harmonic Forcing.** The above introductory example has shed some light on the response behavior of the Ginzburg–Landau equations to external forcing. Even though the signal has demonstrated amplification and frequency selection of the linear system, a more general analysis is pursued that parametrizes the input-output behavior more precisely.

For this reason, we will consider two distinct input signals: an impulsive signal applied at a specified location  $x_w=-11$ , which will trigger what is referred to as the impulse response, and a harmonic signal, again applied at a given location, which yields the frequency response of the linear system.

For the impulsive response we thus assume

$$u(t) = \delta(t) \quad (28)$$

which, according to Eq. (27), results in

$$y(t) = Ce^{At}B = g(t) \quad (29)$$

The spatial localization of the impulsive input signal is contained in the matrix  $B$  (see Eq. (A4a)). For  $C=I$ , the above solution (29) represents the Green's function of the Ginzburg–Landau equation. It forms the fundamental solution of the linear system since particular solutions to more general external excitations can be constructed by a simple convolution of the input signal with

the Green's function. The input-output system (23) is defined as stable if and only if the impulse response (29) decays as time tends to infinity. Consequently, the convectively unstable flow is input-output stable, which is in contrast to the globally unstable flow where an impulse will trigger the growth of an unstable global mode with a well-defined frequency. For the convectively unstable case, the state impulse response  $q(t)=e^{At}B$  for a pulse introduced at  $x_w=-11$  is displayed in Fig. 12(a); the impulse response (29) is shown in Fig. 12(b). We observe the rise of a wavepacket with a distinct spatial wavenumber and propagation speed. As expected from the introductory example (Fig. 5), the amplitude of the wavepacket grows throughout the unstable do-

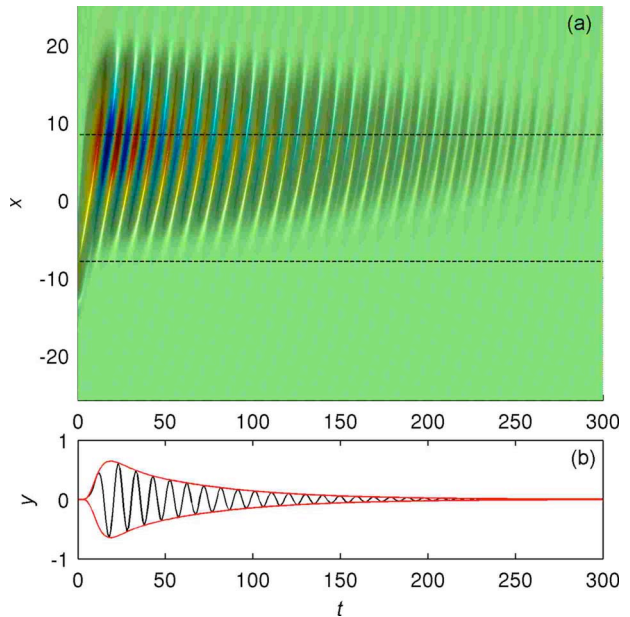


**Fig. 12 Impulse response of the Ginzburg–Landau equation:** (a) The state response to an impulse introduced at  $t=0$  and  $x_w=-11$ . (b) The impulse response at branch II. The convective character of the instability is evident: A wavepacket grows as it enters the unstable domain but is gradually convected away from this domain before it begins to decay.

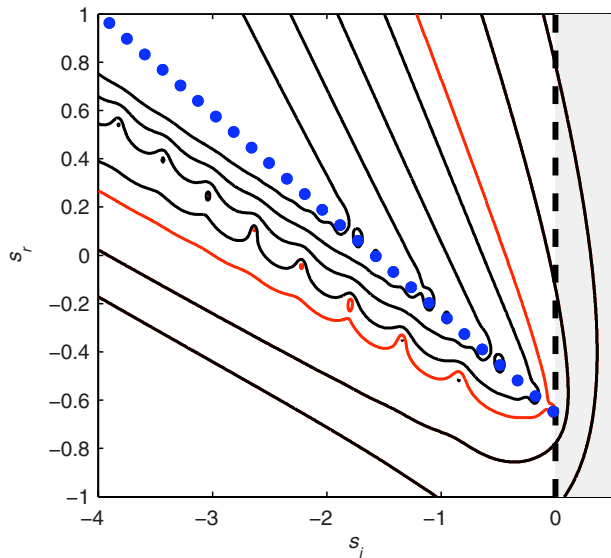


**Fig. 13** Input-output pseudospectra where the black transfer function contour levels are  $\{10^0, 10^1, 10^3, 10^4, 10^5, 10^6\}$ . The red contour (with level 208) represents the largest contour value that crosses the imaginary axis. The blue symbols indicate the eigenvalues of  $A$ .

main before it decays as the wavepacket passes branch II. For larger times, only the remnants of the wavepacket near branch II are observed.

The impulsive signal  $u(t)=\delta(t)$  contains all temporal frequencies with equal amplitude. It is thus ideally suited to extract and analyze a frequency selection behavior from an unbiased input. On the other hand, we could choose an input signal with only one frequency (rather than all frequencies), i.e.,

$$u(t)=e^{st}, \quad s \in \mathbb{C} \quad (30)$$

Inserting the above input into Eq. (27), assuming  $A$  is globally stable and  $t=\infty$ , yields

$$y(t)=\int_0^\infty g(\tau)e^{s(t-\tau)}d\tau=\underbrace{\int_0^\infty g(\tau)e^{-s\tau}d\tau e^{st}}_{G(s)}=|G(s)|e^{(st+\phi)} \quad (31)$$

We can identify the transfer matrix of dimension  $r \times p$

$$G(s)=C(sI-A)^{-1}B, \quad s \in \mathbb{C} \quad (32)$$

as the Laplace transform of the impulse response  $g(t)$ . Due to the linear nature of the Ginzburg–Landau equation, an input  $e^{st}$  will generate an output with the same frequency but with a phase shift  $\phi=\text{Arg } G(s)$  and an amplitude of  $|G(s)|$ . Since  $G(s)$  is usually a rectangular matrix, the amplitude is defined as

$$|G(s)|=\sigma_1 \quad (33)$$

where  $\sigma_1\{\cdot\}$  denotes the largest singular value of  $G(s)$ . The transfer function  $G(s)$  fully describes the input-output behavior of the system, whereas the state-space formulation (23) describes the dynamics of flow.

The transfer function can be regarded as a generalization of the resolvent (21) introduced earlier. In fact, the pseudospectra in Fig. 10 are contours of  $|G(s)|$  for the case  $B=I$ , which corresponds to a uniform distribution of the input, and  $C=F$  (where  $M=F^H F$ ), which corresponds to the measurement of the flow energy. As discussed in Sec. 2.3, the contours represent locations in the complex plane where approximate eigenvalues of  $A$  can be found for a given error norm ( $\epsilon=1/|G(s)|$ ). Figure 13 displays the pseudo-

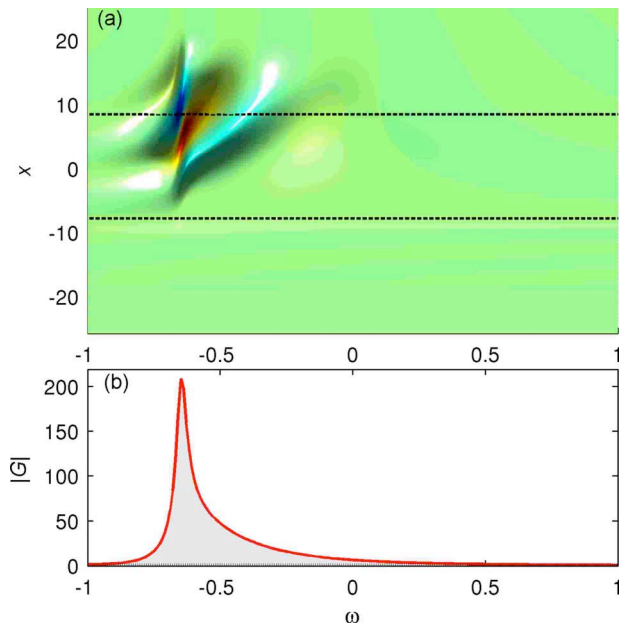


**Fig. 14** (a) The state response to harmonic forcing located upstream of branch I (lower of the two dashed lines). The largest response is at branch II (upper dashed line) for  $\omega=-0.65$ . (b) The frequency response, where the output is a Gaussian function (see Appendix), is located at branch II. In the gray area, all forcing frequencies are amplified in the unstable domain, and all other frequencies are damped illustrating a filtering effect. This response corresponds to the thick dashed line representing the imaginary axis in the pseudospectra plot in Fig. 13, and the peak value  $\|G\|_\infty=208$  corresponds to the red contour level.

spectra of the input-output system with  $B$  defined as in Eq. (A4) and  $C=F$ . In this case, the contour levels correspond to the response amplitude of the output for a unit amplitude input of the form  $e^{st}$ .

As an example, we will concentrate on a purely harmonic forcing and set  $s=i\omega$ . The response of the linear system to this type of excitation is given by the expression

$$G(i\omega)=C(i\omega I-A)^{-1}B, \quad \omega \in \mathbb{R} \quad (34)$$

and the largest response to a harmonic input can be defined as the maximum value of  $|G(i\omega)|$ ,

$$\|G\|_\infty=\max_\omega|G(i\omega)| \quad (35)$$

A remark on the choice of notation seems necessary: In Sec. 2.3, we defined the energy norm of the state vector  $q(t)$  as  $\|q\|_M^2=q^H M q$ , whereas the definition (35) of  $\|G\|_\infty$  represents a norm of all stable transfer functions in the complex frequency space.

For normal systems the largest response to harmonic forcing is proportional to the distance of the real part of the largest eigenvalue of  $A$  to the imaginary axis, i.e.,

$$\|G\|_\infty \sim 1/|\text{Re}(\lambda_1)| \quad (36)$$

For non-normal systems, however, the response of the system can be substantial even though the forcing frequency is nowhere close to an eigenvalue. The largest response  $\|G\|_\infty$ , in this case, is proportional to the largest value of the contour  $|G(s)|$  that crosses the imaginary axis.

This feature is exemplified on the Ginzburg–Landau equation in Figs. 13 and 14. The state response (i.e., the special case with  $C=I$ ) to spatially localized harmonic forcing at  $x_w=-11$  is shown in Fig. 14(a). The largest response is obtained for a frequency of  $\omega$

$=-0.65$ , and the location of the most amplified response in space is—not surprisingly—in the vicinity of branch II. In Fig. 14(b), the frequency response  $|G(i\omega)|$  is shown, which corresponds to the dashed line in the contour plot of Fig. 13. The peak of this response  $\|G_c\|_\infty=208$  is associated with the red contour in the pseudospectra plot (Fig. 13). The response computed from the distance to the nearest eigenvalue (36) has a value of only 56. It is thus confirmed that the frequency response for non-normal systems is substantially larger than what can be inferred from the distance of the forcing frequency to the nearest eigenvalue.

**3.2 Stochastic Forcing.** Under realistic conditions, we rarely possess the exact knowledge of the disturbances influencing the flow system, and it is therefore essential to account for a certain amount of uncertainty. In this section, we present fundamental techniques to characterize the response behavior within a statistical framework. This framework also gives insight into inherent stability properties of the flow [6,71], as, for example, in the case of channel flow studied in Refs. [9,69,72] and boundary layer [73]. When a fluid system is externally excited by stochastic disturbances, its response is best characterized by the state statistics, for instance, the root mean square (rms) values of the velocity components, the mean energy, or two-point correlations. In the context of aerodynamic flows, stochastic excitation can be attributed, among others, to freestream turbulence, wall roughness, or incident acoustic waves.

A naive statistical analysis may consist of performing a large number of simulations by choosing sample realizations of the forcing and by subsequent averaging of the resulting flow quantities to obtain the desired statistics. A more direct approach involves the derivation of evolution equations for the statistical properties, e.g., two-point correlations, of the flow quantities. For linear systems, it is possible to solve directly for the two-point correlations of the flow quantities in terms of the two-point correlations of the external excitation. The key equation relating second-order statistics of the excitation to second-order statistics of the state is the Lyapunov equation. In this section, we will derive the Lyapunov equation and give examples of how to extract relevant information from its solution.

An introductory example can be seen in Fig. 15(a) where the temporal evolution of the state energy is displayed as a random forcing with zero mean and unit variance applied upstream of branch I. The results of five simulations are shown. Due to the stochastic nature of forcing, each simulation yields different results but, nevertheless, reveals a general trend: No energy is observed at the beginning of each simulation (since the initial condition is identically zero), but considerable energy levels are reached after an initial transient of approximately 100 time units and a quasisteady regime in which the energy fluctuates about a mean value are established. Because of this observed noise amplification, convective unstable flows are also referred to as noise amplifiers. Furthermore, the dashed line shows the average of 50 simulations, representing the evolution of the mean energy. This curve is compared to the mean energy (red solid line) computed from the algebraic Lyapunov equation; this means energy level is increasingly better approached as the number of simulations comprising the average is increased.

Although the above experiment already demonstrates the amplification behavior of a convectively unstable linear system driven by stochastic forcing, the relation between the forcing covariance and the resulting state covariance will be established next.

We again consider the linear system given by Eq. (23), now driven by a stochastic process  $u(t)$ , i.e., a random time-varying input signal. We assume that  $A$  is globally stable but convectively unstable. To simplify the analysis, we also assume that the random variable  $u$  is normally distributed, i.e., that the probability density function of the stochastic process is Gaussian, completely characterized by its mean and its variance.

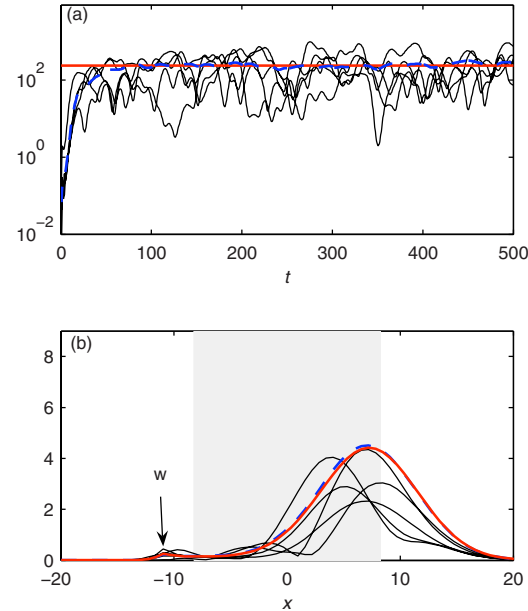


**Fig. 15 The response to stochastic forcing.** (a) The evolution of the state energy for five different simulations (black lines), the mean state energy given by the solution of the algebraic Lyapunov equation (red solid line), and the energy averaged over 50 simulations (thick dashed line). (b) The thick red line shows the rms value of the Ginzburg–Landau equation when excited by random forcing  $w$  at the location marked with an arrow. Five representative snapshots of the response to this forcing are shown by black thin lines; the average over 50 simulations is displayed by a thick blue dashed line.

To represent the mean and the variance of a random variable, we introduce the expectation operator  $\mathcal{E}$ . The mean of a scalar random variable  $\xi$  is then  $m=\mathcal{E}\{\xi\}$ ; its variance is the quadratic expression  $\sigma^2=\mathcal{E}\{\xi\xi^H\}$ . From a statistical point of view,  $\mathcal{E}$  can be thought of as an averaging operator (for example, the action of an integral in time.)

We can similarly characterize the covariance of two random variables  $\xi$  and  $\eta$  as  $P_{\xi\eta}=\mathcal{E}\{\xi\eta^H\}$ . The covariance of two random variables gives information about the degree of similarity of the two signals. The above definition of the covariance is readily extended to vectors of random variables. The covariance of two random vector variables  $f(t)$  and  $g(t)$  of dimension  $n$  is simply the  $n \times n$  matrix,

$$P_{fg}(t)=\mathcal{E}\{f(t)g(t)^HM\} \quad (37)$$

Using the energy weight matrix  $M$ , we recover the kinetic energy of a state by simply taking the trace of the covariance matrix,

$$E(t)=\mathcal{E}\{\text{tr}(q(t)q(t)^HM)\}=\text{tr}(P_{qq}) \quad (38)$$

Furthermore, the diagonal elements of  $P_{qq}$  are the variance of the individual elements of  $q(t)$ . In particular, we define the rms value of the disturbance as

$$q_{\text{rms}}(t)=\sqrt{\text{diag}\{P_{qq}\}} \quad (39)$$

From Eqs. (38) and (39), it is clear that the covariance of the state contains all the essential statistics that is necessary for evaluating the response to stochastic forcing. We now return to our dynamical system (23) and derive an explicit expression of the state covariance in terms of the forcing covariance. For simplicity, we will assume that the applied forcing is uncorrelated in time, that is, it is a temporal white-noise process:

$$\mathcal{E}\{u(t)u(t')^H M\} = WM \delta(t-t') \quad (40)$$

where  $t$  and  $t'$  are the two instances in time, and  $W$  denotes the spatial covariance of  $u$ . For example, if  $u$  is a vector of random variables,  $W_{ij} = \mathcal{E}\{u_i u_j^H\}$ .

To derive an evolution equation for the covariance of the state, we start with the expression describing the time evolution of the state forced by  $u$  (i.e., Eq. (27) with  $C=I$ ),

$$q(t) = \int_0^t e^{A(t-t')} Bu(t') dt' \quad (41)$$

As before, we have assumed a zero initial condition  $q_0=0$ .

We begin with the definition of the covariance matrix  $P_{qq}$  of the state at time  $t$ :

$$\begin{aligned} P &= \mathcal{E}\{q(t)q(t)^H M\} \\ &= \int_0^t \int_0^t e^{A(t-t')} B \underbrace{\mathcal{E}\{u(t')u(t'')^H M\}}_{WM \delta(t'-t'')} B^H e^{A^H(t-t'')} dt' dt'' \\ &= \int_0^t e^{A(t-t')} B W B^+ e^{A^+(t-t')} dt' \end{aligned} \quad (42)$$

where we have used the fact that  $u$  is uncorrelated in time and omitted the subscript “ $qq$ .” We can differentiate this last expression in Eq. (42) with respect to time to obtain an evolution equation for  $P$  of the form

$$\dot{P} = AP + PA^+ + BWB^+, \quad P(0) = 0 \quad (43)$$

In this expression  $\dot{P}$  denotes the time derivative of the covariance matrix. The above equation is referred to as a differential Lyapunov equation. Given the covariance  $W$  of the forcing term  $u$ , we obtain the time evolution of the state covariance  $P$ . If the system  $A$  is asymptotically stable and, furthermore,  $A$ ,  $W$ , and  $B$  are time independent, the stochastically driven system relaxes after an initial transient into a statistical steady state. To obtain this steady state, we set  $\dot{P}=0$  and recover the algebraic Lyapunov equation

$$AP + PA^+ + BWB^+ = 0 \quad (44)$$

This statistical steady state is of interest if we study a system that is exposed to external forcing for a long-time horizon, e.g., the flow over a wing under cruise conditions. We like to emphasize that despite the presence of a steady statistical state, the state vector of the system, as well as the external forcing, is varying in time.

To illustrate the above statistical description of the system dynamics, we revisit the Ginzburg–Landau equation forced at the upstream edge of the convectively unstable region where we apply the external excitation of Gaussian form shown in Eq. (A4a), with  $u(t)$  as a scalar white-noise process with zero mean and unit variance  $W=1$ . The covariance of the state obtained by solving the algebraic Lyapunov equation [74] is depicted in Fig. 16. The rms value of this state covariance is shown with a red line in Fig. 15(b) and the gray area marks the region of convective instability. In addition, we have represented the instantaneous state of five realizations of the forcing and the mean of 50 of these realizations, as we did in Fig. 15(a) for the total energy evolution in time. We see that the average of 50 realizations is close to the mean obtained from the Lyapunov equation, but a sample set of 50 realization is not yet enough for a converged statistical result. We will see more examples of this kind in the control section where we will quantify the performance of the controller using mean energy.

We conclude this section by stressing that transient growth mechanisms in hydrodynamic stability theory and the spatiotemporal evolution of disturbances can be recast into an input-output

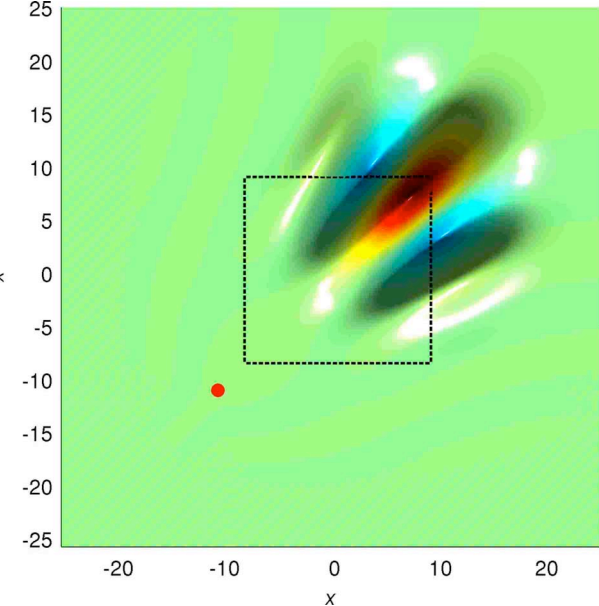


**Fig. 16** The state covariance/controllability Gramian  $P$  of the Ginzburg–Landau equation. The Gramian describing how the state components are influenced by an input corresponds in a stochastic framework to the state covariance for white noise as input. The red circle signifies the forcing location ( $x_w=-11$ ), and the dashed box marks the region of instability. The states that are most sensitive to forcing, and thus controllable, are located downstream, at branch II.

framework. For example, in this framework, the output signal  $y(t)$  to random, impulsive, or harmonic inputs shown in Figs. 11, 12, and 14, respectively, exhibits an initial growth in time before the signal either decays to zero or stabilizes around a steady state.

**3.3 Controllability and Observability.** An important issue in the analysis of linear systems in state-space form concerns the mapping between input signals and the state vector and between the state vector and the output signals. Since for many realistic configurations the matrices  $B$  and  $C$  are rectangular, reflecting the fact that we force the system only at a few points in space and/or measure the system only at a limited number of sensors, we need to address the topic of controllability and observability [68].

In this section, we will characterize the controllability and observability of a system in terms of covariance matrices of the state and the adjoint state, which in this context are called *Gramians*. We will continue to consider one input and one output and assume that  $A$  is stable (subcritical Ginzburg–Landau equation), even though the theory extends to unstable systems as well [75].

**3.3.1 Controllability: The POD Modes.** The controllability of a system is concerned with finding the flow states most easily influenced by a given input. It can be shown [22,76] that the minimum amount of input energy  $\|u\|_2^2$  to bring the state from zero to the given initial condition  $q_0$  is given by the expression

$$q_0^H P^{-1} q_0 \quad (45)$$

where  $P$  is the unique  $n \times n$  matrix

$$P = \int_0^\infty e^{A\tau} BB^+ e^{A^+\tau} d\tau \quad (46)$$

referred to as the *controllability Gramian* (for a derivation of this result in terms of an optimal control problem, see Ref. [22]). Also note that the adjoint operators with superscript “ $+$ ” are related to the conjugate transpose  $H$  according to Eq. (25).

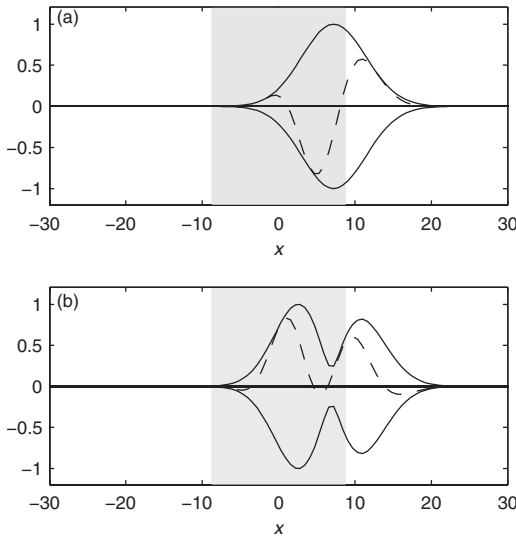


**Fig. 17** The first (a) and second (b) POD modes obtained from an eigenvalue decomposition of the controllability Gramian in Fig. 16. Note that these modes are orthogonal. The absolute value is shown in solid and the real part in dashed. The gray area marks the region of instability.

Since for linear systems the state for an impulsive input at any given time is  $q(t)=e^{At}B$ , we recognize that the controllability Gramian (46) equals an infinite-horizon state covariance (42) with covariance  $W=I$ . This is not very surprising since one can interpret white noise as a set of impulse inputs that are uncorrelated in time. Furthermore, assuming  $A$  is stable, the controllability Gramian can be computed by solving the algebraic Lyapunov equation (44). In Fig. 16, the controllability matrix of the Ginzburg–Landau equation is shown graphically. The state components that respond to an input located just upstream of the unstable region are situated downstream of the unstable domain.

By diagonalizing the matrix  $P$ , we obtain a measure of controllability for each component of the state vector. The diagonalization of the covariance matrix or, in the linear framework, the controllability Gramian is commonly referred to as the POD [77] but is also known as empirical eigenfunction (EOF) decomposition, Karhunen–Loëve decomposition, or principal component analysis (PCA). The eigenvectors and eigenvalues of  $P$  are given by

$$P\phi_i = \lambda_i \phi_i, \quad \lambda_1 \geq \dots \geq \lambda_n \geq 0 \quad (47)$$

Since  $P$  is positive semidefinite, the eigenvalues are real and positive and the eigenvectors are orthogonal. The first two POD modes of the Ginzburg–Landau equation are shown in Fig. 17. Traditionally, the interpretation of these modes is that they represent decorrelated energy-ranked flow states. For example, the first POD mode  $\phi_1$  is the most energetic structure in the flow containing  $\lambda_1/\sum_{i=1}^n \lambda_i$  of the total flow energy. From a linear system's point of view, POD modes can be considered as the most controllable structures of the system for a given input. In this case the eigenvalue  $\lambda_i$  is a measure of how much the state  $\phi_i$  is influenced by the input. In particular, if  $P$  is rank deficient, there exists a zero eigenvalue,  $\lambda_i=0$ , which would mean according to Eq. (45) that the energy required to influence the corresponding state is infinite. If  $P$  is not rank deficient, we say that  $(A, B)$  is controllable.

**3.3.2 Observability: The Adjoint POD Modes.** The POD modes capture the response to input and thus span a controllable subspace of the state space. Equally important in the input-output analysis is to take into account the observable subspace by considering the relation between the outputs and flow states. A similar analysis as in Sec. 3.3.1 for POD modes is thus performed, but

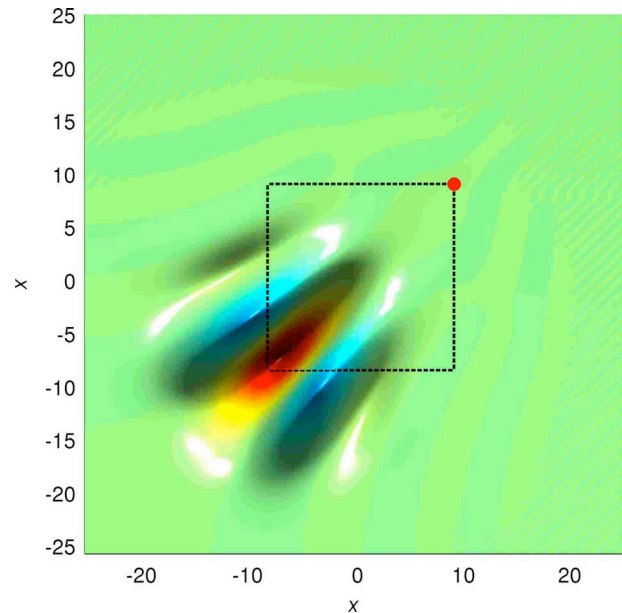


**Fig. 18** The observability Gramian  $Q$  of the Ginzburg–Landau equation. The red circle marks the location of the output  $C$  at branch II. The initial states that contribute most to the output are located upstream, at branch I.

this time for the adjoint system (24). Comparing the direct state-space equations (23) with their corresponding adjoint state-space equations (24), we observe that the output of the direct equations is related to the input of the adjoint equations.

The observability of a system is concerned with finding the initial conditions  $q_0$  that will produce the largest output energy. For zero input, the solution to the state-space equations is

$$y = Ce^{At}q_0 \quad (48)$$

The output energy is then given by

$$\|y\|_2^2 = q_0^H Q q_0 \quad (49)$$

where the *observability Gramian*

$$Q = \int_0^\infty e^{A^+ \tau} C^+ C e^{A \tau} d\tau \quad (50)$$

is a unique matrix of dimension  $n \times n$ .

If we note that the impulse response of the adjoint state-space equations (24) is given by

$$r(t) = e^{A^+ t} C^+ \quad (51)$$

the observability Gramian can be written as the state correlation matrix of the adjoint system

$$Q = \mathcal{E}\{rr^H M\} \quad (52)$$

and the Gramian can be computed by solving the algebraic Lyapunov equation

$$A^+ Q + QA + C^+ C = 0 \quad (53)$$

In Fig. 18, the observability matrix of the Ginzburg–Landau equation is shown. The observable components of the state vector are located upstream of the unstable domain when the output location is at branch II (red dot in Fig. 18).

By diagonalizing the observability Gramian,

$$Q\psi_i = \lambda_i \psi_i, \quad \lambda_1 \geq \dots \geq \lambda_n \geq 0 \quad (54)$$

we obtain an orthogonal set of functions called the adjoint POD modes or the most observable modes. These modes are flow struc-

tures that are ranked according to their contribution to the output energy. The corresponding eigenvalues  $\lambda_i$  provide a means to measure how observable the corresponding eigenvectors are. If there exist zero eigenvalues,  $\lambda_i=0$ ,  $Q$  is rank deficient, which means according to Eq. (49) that the corresponding adjoint POD mode does not contribute to sensor output. If  $Q$  has full rank, we say that  $(C, A)$  is observable.

It should be evident that in order to build an effective control system, both sufficient controllability and observability have to be established. Only in this case will the actuation have an appreciable effect on the flow system whose response, in turn, will be detectable by the sensors. Without adequate controllability or observability the flow of information from the system's output to the system's input will be compromised, and any control effort will be futile. Within the LQG-based feedback control framework, the controller will always stabilize the system if the unstable global eigenmodes are both controllable and observable. We will show how the controllability and observability of global eigenmodes can be determined in Sec. 4.

## 4 Model Reduction

Any type of significant flow control applied to the discretized two- or three-dimensional Navier–Stokes equations requires some form of model reduction. Model reduction is concerned with the transformation of a system with a large number of degrees of freedom to an approximately equivalent system of markedly smaller size. The term “approximately equivalent” is often difficult to quantify and usually encompasses a measure of preservation of important system characteristics under the model reduction transformation. In this sense, model reduction becomes problem dependent: for example, a transformation that preserves the inherent dynamics of the system may be inappropriate in capturing the input–output behavior.

Model reduction techniques for fluid systems typically rely on physical insight into the specific flow situation rather than on a systematic approach detached from the application. For instance, for spatially invariant systems, it is possible to decouple the linear state-space equations in Fourier space. Control, estimation, and other types of optimization can then be performed independently for each wavenumber and then transformed back to physical space. This approach has been adopted in Refs. [12–16,19].

The model reduction (or projection) technique [76,78] discussed in this paper involves three steps.

The first step consists of finding an expansion basis  $\{\phi_i\}_{i=1}^r$  that spans an appropriate subspace of order  $r$  of the state space of order  $n$ , with  $r \ll n$ . We will present and compare three different subspaces using the Ginzburg–Landau equation: the subspace spanned by the least stable global eigenmodes, POD modes, and the balanced modes (described in Secs. 4.1–4.3).

In a second step, the state-system given by Eq. (23) is projected onto this subspace yielding the reduced-order model

$$\dot{\kappa}(t) = \hat{A}\kappa(t) + \hat{B}u(t) \quad (55a)$$

$$y(t) = \hat{C}\kappa(t) \quad (55b)$$

$$\kappa(0) = \kappa_0 \quad (55c)$$

When the expansion basis is nonorthogonal, we can use a set of adjoint modes  $\{\psi_i\}_{i=1}^r$  associated with  $\{\phi_i\}_{i=1}^r$ , to obtain the entries of  $\kappa$ ,  $\hat{A}$ ,  $\hat{B}$ , and  $\hat{C}$ ,

$$\hat{\kappa}_i = \frac{\langle q, A\phi_i \rangle}{\langle \psi_i, \phi_i \rangle} \quad (56a)$$

$$\hat{A}_{i,j} = \frac{\langle \psi_i, A\phi_j \rangle}{\langle \psi_i, \phi_i \rangle} \quad (56b)$$

$$\hat{B}_i = \frac{\langle \psi_i, B \rangle}{\langle \psi_i, \phi_i \rangle} \quad (56c)$$

$$\hat{C}_i = C\phi_i \quad (56d)$$

with  $i, j = 1, \dots, r$ . The term  $\langle \psi_i, \phi_i \rangle$  is a normalization factor that we choose such that  $\|\phi_n\| = \|\psi_n\| = 1$  and is smaller than 1 if the modes are nonorthogonal, that is,  $\psi_i \neq \phi_i$ . The subscript  $M$  in the above inner products is omitted for brevity and we have assumed that  $B$  is a column vector and  $C$  is a row vector, i.e., we continue to consider one input and one output.

The third and final step consists of estimating the error of the reduced-order model (55). For control purposes, it is not necessary for the reduced-order model to capture the entire dynamics described by the general state-space formulation (23), rather it suffices to accurately capture the input–output behavior described by the transfer function  $G(s) = C(sI - A)^{-1}B$ . It thus seems reasonable to estimate the error of a reduced-order system by comparing the norms of the transfer function (34) of the full system  $G$  and the reduced system  $G_r = \hat{C}(sI - \hat{A})^{-1}\hat{B}$ , e.g.,  $\|G - G_r\|_\infty$  [23,78,79]. This is equivalent to calculating the difference of the peak values of the frequency response between the two models.

**4.1 Global Modes and Input/Output Residuals.** Global modes (Figs 7(a) and 7(b)) preserve the dynamical characteristics of the system matrix  $A$ . Model reduction using global modes simply consists of an expansion of the state vector  $q$  into the leading global eigenmodes (10b), where eigenmodes with substantial decay rates will be neglected. By this process, the resulting new system matrix  $\hat{A}$  in Eq. (55) will consist of a diagonal matrix of the retained global eigenvalues. The new reduced state vector  $\kappa$  is given by the eigenfunction expansion coefficients, and the expansion coefficients of  $B$  (56c) and  $C$  (56d) are called the *controllability modal residuals* and the *observability modal residuals*, respectively (see also Ref. [11]).

It is clear that if  $\langle \psi_i, B \rangle$  is zero in Eq. (56c), we will not be able to act on the corresponding state component  $\kappa_i$  and therefore on the global mode  $\phi_i$ . Thus, we can use the controllability modal residual as a measure of controllability of the global mode by considering the amount of overlap between the support of the input and the support of the corresponding adjoint global mode. If this overlap is zero, the global mode is not controllable [30,34].

A similar derivation based on Eq. (56d) shows that in order for  $(C, A)$  to be observable, the spatial support of the sensor and the support of the global mode must overlap. If  $\hat{C}_i = C\phi_i$  is zero, we will not be able to detect the eigenmode  $\phi_i$  using a sensor characterized by  $C$ . This eigenmode is thus unobservable.

Owing to the term  $\langle \psi_i, \phi_i \rangle$  in the denominator of Eq. (56c), additional attention has to be paid to the system's sensitivity due to non-normal effects: the forcing response or controllability of  $\phi_i$  is inversely proportional to  $\langle \psi_i, \phi_i \rangle$ , i.e., the separation of global and adjoint modes. This separation is illustrated in Fig. 19(a), where the spatial support—defined as the region where the amplitude of a particular mode is larger than 2% of its maximum amplitude (see also Ref. [33])—of the first 20 global and adjoint modes is shown. We see that the global modes only span a small part of the domain, which is located near and downstream of the unstable domain (green dashed line), whereas the corresponding adjoint modes are located upstream of the unstable domain (red dashed line); this results in a large sensitivity,  $\langle \psi_i, \phi_i \rangle \ll 1$ .

In Fig. 20, we display the controllability as the number of global modes is increased, together with the numerator and denominator of expression (56c). Whereas the numerator represents a measure of overlap between the input and the adjoint global modes, the denominator measures the degree of non-normality. The marked rise in controllability as more global modes are added

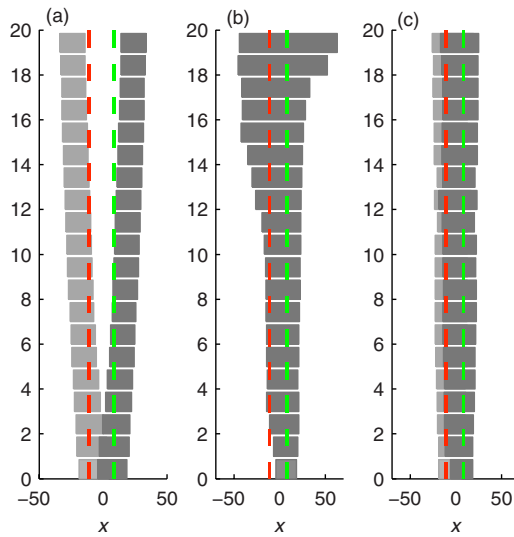


**Fig. 19** The spatial support of the first 20 global (a), POD (b), and balanced modes (c). The spatial support is defined as the region where the amplitude of a particular mode is larger than 2% of its maximum amplitude. The location of the input (just upstream of branch I) and output (at branch II) is marked with red and green dashed lines, respectively. The global modes span only the region around branch II. The first POD modes (b) are located at branch II, even though the higher modes quickly recover the input. The balanced modes (c) cover the region between the input and output with only two modes. The areas marked with light gray in (a) and (c) represent the spatial support of the adjoint modes for the global and balanced modes. The spatial separation in  $x$  of the direct and adjoint modes, shown in (a) for global modes, is absent in (b) for the balanced modes.

is thus a compound effect of these two components. It illustrates that non-normal systems can be very sensitive to the external perturbation environment and that it is possible to manipulate the flow using very small actuator effort.

An upper limit of the error for reduced-order models based on global modes is given by [76,80]

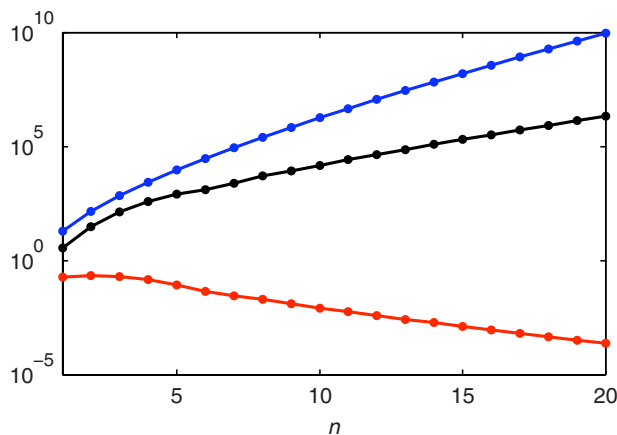


**Fig. 20** The controllability modal residuals (black line) of the first 20 global modes given by Eq. (56c), which is the product of the overlap of the actuator and adjoint mode  $\langle \psi_i, B \rangle$  (red) and the sensitivity defined by  $(\langle \psi_i, \phi_i \rangle)^{-1}$  (blue). Although the overlap of the spatial support of the actuator decreases for higher modes, the controllability still increases due to the rapid growth of the receptivity of higher modes to forcing, quantified by the inverse of  $\langle \psi_i, \phi_i \rangle$ .

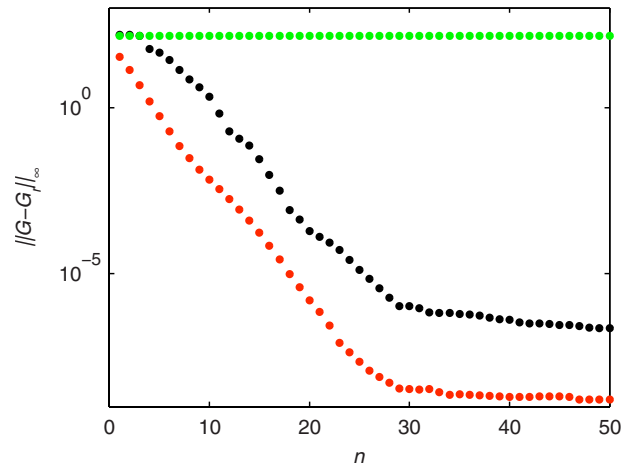


**Fig. 21** Model reduction error of the POD (black), balanced (red), and global (green) modes. For the balanced modes, the error always decays by increasing the number of modes, in contrast to the error of POD modes. The error does not decay at all for the first 50 global modes due to the failure to project the input  $B$  located upstream of branch I onto the global eigenmodes located close and downstream to branch II.

$$\|G - G_r\|_\infty \leq \sum_{i=r+1}^n \frac{|\hat{C}_i \hat{B}_i|}{|\text{Re}(\lambda_i)|} \quad (57)$$

From the above expression, it is evident that choosing a subspace based on the criterion of dominant eigenvalues may not be appropriate if one wishes to approximate the input-output behavior. The reason is that the error norm (57) depends on the matrices  $B$  and  $C$ . Although the eigenvalues may exhibit substantial decay, for highly non-normal systems  $\hat{B}$  is large yielding a large model reduction error, as shown in Fig. 21 using green circles.

In Fig. 22, we compare the frequency response of the full model  $|G(i\omega)|$  of order  $r=220$  (blue dashed line) to the frequency response of the reduced models  $|G_r(i\omega)|$  of order  $r=2, 4$ , and  $6$  (green solid line). As before, the input  $B$  (at branch I) is located upstream and the output  $C$  (at branch II) downstream. The frequency response of the reduced models shows a large deviation from the true frequency response, even as the number of included modes is increased.

**4.2 POD Modes.** For an improved transfer behavior of the reduced model, we can base our subspace on the response of the linear system to external forcing. In this case, both the system matrix  $A$  and the control matrix  $B$  determine the dynamics of the driven system. To reduce a driven model, we will expand the state vector into the POD modes (47) (Fig. 17). The expansion in POD modes will be truncated at a convenient level that results in a significantly lower-dimensional system matrix but still retains the most energetic structures. These modes are ideal in detecting and extracting coherent fluid structures in a hierarchical manner that is based on their contribution to the overall perturbation energy of the flow. However, for control and input-output behavior, low-energy features that are not captured by this expansion may be critically important.

We like to point out that the controllable subspace adequately spans the *response* to inputs but not necessarily the inputs themselves. This is illustrated in Fig. 19(b), where the spatial support of the first 20 POD modes are shown. The first POD modes capture the largest structures, located at branch II; however, in contrast to the global modes, the higher modes eventually cover the entire unstable domain including our input location. For this reason, the error norm shown with black circles in Fig. 21 is not decreasing for the first three POD modes; only when the fourth

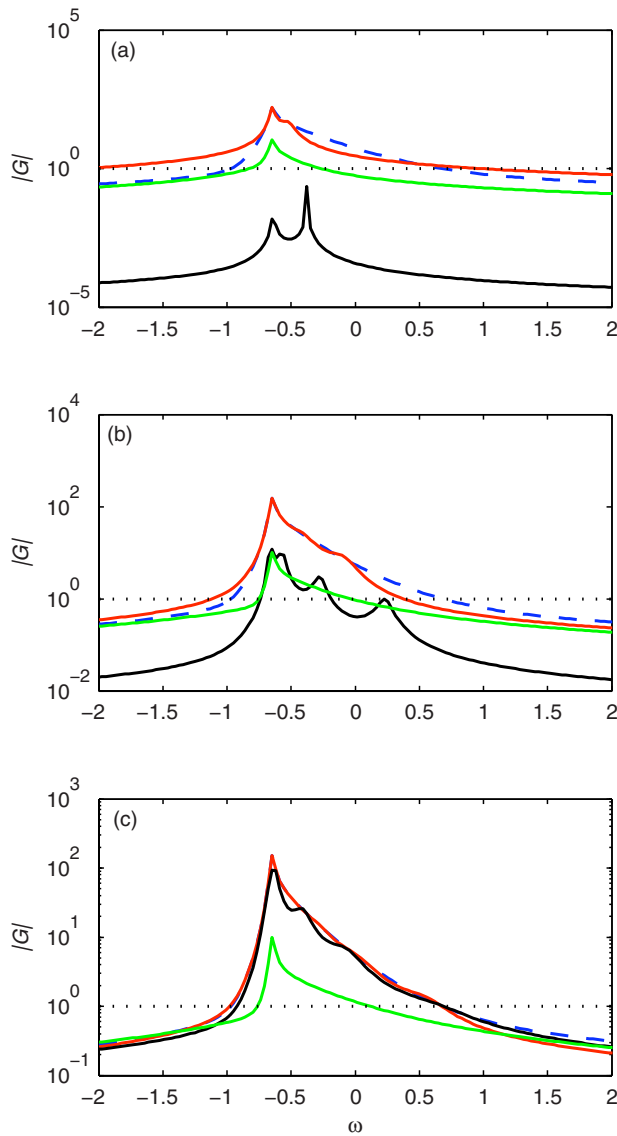


**Fig. 22** Comparison of the frequency response of the full Ginzburg–Landau equation with three reduced-order models. The blue dashed lines represent the full model of order  $n = 220$ . The performance of reduced-order models based on  $r = 2, 4$ , and  $6$  modes are shown in the (a), (b), and (c), respectively. The red lines represent the balanced modes, the black lines represent the POD modes, and green lines represent the global eigenmodes. We observe that the balanced modes capture the peak value of the frequency response, which represents the main characteristic of the input-output behavior. The approximation of the frequency response for the open-loop case is unsatisfactory for POD models of orders 2 and 4 and for all global-mode models.

mode, which captures some of the input structure, is included in the expansion basis does the error norm begin to decrease. An explicit error estimate does not exist for POD modes; only after computing the frequency response of the two systems can one determine the error (given by the difference of the peak values in the frequency response).

Finally, in Fig. 22 the frequency response of the POD-based reduced model (black line)  $|G_r(i\omega)|$  of order  $r=2, 4$ , and  $6$  is observed to gradually approach the response of the full model.

**4.3 Balanced Modes.** The third subspace is based on *balancing* the system and involves the three matrices  $A$ ,  $B$ , and  $C$ . It is based on the idea of reducing the dimensions of the original sys-

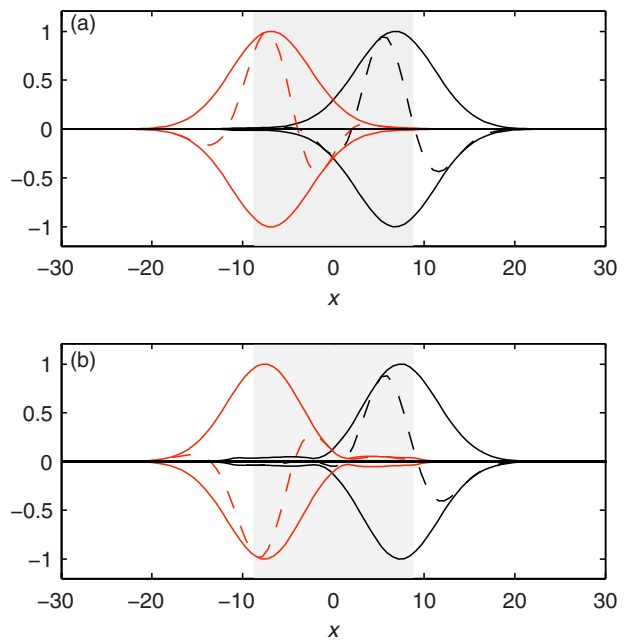


**Fig. 23** The first (a) and second (b) balanced modes. The modes are nonorthogonal and the adjoint balanced modes are shown in red. The absolute value is shown in solid and the real part in dashed. The gray area marks the region of instability.

tem by (i) removing the redundant states for characterizing the input-output behavior—the uncontrollable and unobservable states—and (ii) by removing the states that are nearly uncontrollable and unobservable. This technique of model reduction is referred to as balanced truncation [81].

The balanced modes  $\{\phi_i\}_{i=1}^r$  are defined as the eigenvectors of the product of the two Gramians,

$$PQ\phi_i = \phi_i\sigma_i^2, \quad \sigma_1 \geq \dots \geq \sigma_r \geq 0 \quad (58)$$

The eigenvalues  $\sigma_i$  are called the Hankel singular values (HSVs). First two balanced modes are shown in Fig. 23.

To illustrate what *balancing* refers to, let us consider the projection of the Gramian matrices  $P$  and  $Q$  on a set of modes, for instance, any of the modes introduced in this section. The projected matrices, denoted by  $\hat{P}$  and  $\hat{Q}$ , have the elements

$$\hat{P}_{i,j} = \langle \psi_i, P\psi_j \rangle \quad (59a)$$

$$\hat{Q}_{i,j} = \langle \phi_i, Q\phi_j \rangle \quad (59b)$$

where  $\psi_i$  denotes the adjoint mode associated with  $\phi_i$ . Balancing refers to the fact that if  $\hat{P}$  and  $\hat{Q}$  are obtained from a projection onto balanced modes, they become diagonal and equal to the Hankel singular values, i.e.,

$$\hat{P} = \hat{Q} = \Sigma = \text{diag}(\sigma_1, \dots, \sigma_r) \quad (60)$$

The balanced modes are flow structures that are ranked according to their contribution to the input-output behavior. These modes are influenced by the input and, in turn, influence the output by the same amount, given by the corresponding Hankel singular values  $\sigma_i$ .

A very attractive feature of balanced truncation is the existence of an a priori error bound that is of the same order as the lowest bound achievable for any basis,

$$\sigma_{r+1} < \|G - G_r\|_\infty \leq 2 \sum_{j=r+1}^n \sigma_j \quad (61)$$

In contrast to Eq. (57), the above error norm is independent of the input and output matrices  $B$  and  $C$ . The error norm for the balanced truncation model in Fig. 21 shows a rapid decay. In Fig. 22, we notice that the performance of balanced reduced-order models (red lines)  $|G_r(i\omega)|$  is very good, and only two balanced modes are required to capture the peak response of the full system.

In summary, we would like to recall that each of the three sets of basis vectors (global modes, POD modes, and balanced modes) span different subspaces of the state space and are therefore suitable for different applications. The spatial support is shown in Fig. 19 for the first 20 modes of each of the three sets. The balanced modes (right plot), by construction, cover the region between the input and the output with very few modes and are thus the appropriate set of functions to accurately capture the input-output behavior of our linear system.

**4.4 The Snapshot Method.** To compute the POD modes or balanced modes, we must first solve Lyapunov equations. This becomes prohibitively expensive as  $n$  exceeds approximately  $10^5$ , which usually is the case when discretizing the Navier–Stokes equations in two or three dimensions. Recently, numerous iterative methods to solve these equations have appeared [76,82].

A different approach to approximate the Gramians without solving the Lyapunov equations—the so-called snapshot-based balanced truncation—has recently been introduced [83,84]. It is based on the snapshot technique first introduced by Sirovich [85] for computing the POD modes. We will demonstrate the method for one input and one output, see Ref. [83] for additional details.

We begin with collecting  $r$  snapshots  $q(t_j)$  at discrete times  $t_1, \dots, t_r$  of the response of the system (23) to an impulse  $\delta(t)$ . These snapshots are gathered as columns in an  $n \times r$  matrix  $X$ , i.e.,

$$X = [e^{A t_1} B, e^{A t_2} B, \dots, e^{A t_r} B] \sqrt{\Delta_r} \quad (62)$$

where  $\Delta_r$  stands for the quadrature coefficients of the time integral in equation (46). Instead of solving the Lyapunov equation (44), we can approximate its solution, i.e., the controllability Gramian  $P$  with

$$P \approx X X^H M \quad (63)$$

If we observe that  $e^{A^+ t} C^+$  is the impulse response of the adjoint state-space equation (24), we can construct an approximation of the observability Gramian  $Q$

$$Q \approx Y Y^H M \quad (64)$$

by collecting a sequence of snapshots of the adjoint impulse response in the  $n \times r$  matrix

$$Y = [e^{A^+ t_1} C^+, e^{A^+ t_2} C^+, \dots, e^{A^+ t_r} C^+] \sqrt{\Delta_r} \quad (65)$$

In the method of snapshots, instead of solving the large  $n \times n$  eigenvalue problem (58), one can form the singular value decomposition of the  $r \times r$  matrix,

$$Y^H M X = U \Sigma V^H \quad (66)$$

The approximate HSVs are given in the diagonal matrix  $\Sigma$ . The normalized balanced modes and the associated adjoint balanced modes are recovered from

$$T = X V \Sigma^{-1/2}, \quad S = Y U \Sigma^{-1/2} \quad (67)$$

Usually the number of snapshots  $r$  is significantly smaller than the number of states  $n$ , which makes this method computationally tractable for systems of very large dimensions.

Figure 24 shows the HSVs for the exact balanced truncation (solving two Lyapunov equations) and the approximate HSVs (using the snapshot method). For improved results, more snapshots

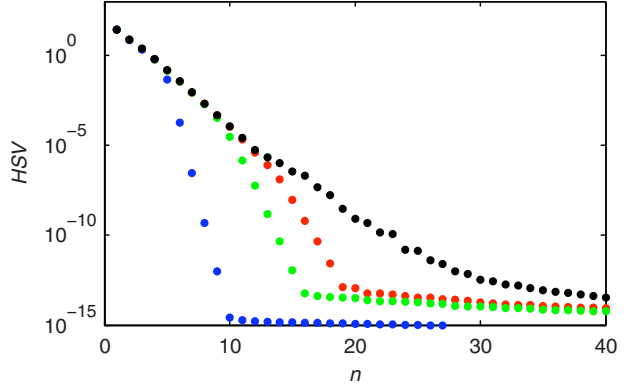


**Fig. 24** Hankel singular values of the approximate balanced truncation are marked with colored symbols and the exact balanced truncation with black symbols. The number of singular values that are correctly captured increases with the number of snapshots (red: 1000; green: 500; blue: 70 snapshots).

may be taken during periods of large transient energy growth and fewer snapshots as the energy decreases. Snapshot-based balanced truncation has been applied to channel flow [86] and to the flow around a pitching airfoil [87].

## 5 Control

The natural extension to the investigations of Secs. 2–4—the response behavior of a linear system to initial conditions and external excitations—is concerned with attempts to manipulate the inherent dynamics of a system or to control it. A substantial body of literature on flow control has accumulated over the past decade, with topics ranging from laminar flow control [88] to control of turbulence [89], and from opposition control [90] to suboptimal [91] and nonlinear control [92–94]. Reviews on the subject of flow control can be found in Refs. [24–27,95,96].

The framework laid out in Secs. 5.1–5.6 falls in the category of *linear feedback control* [20,21,23,80,97]. In particular, our objective is to minimize the perturbation energy resulting from asymptotic or transient instabilities of the uncontrolled system during the transition process in order to suppress or delay turbulence [11,15,17]. Since the disturbance energy growth is initially a linear process [7], it seems prudent to design control schemes for the linearized governing equations. However, linear control has also been applied with considerable success to the full Navier–Stokes equations [12], and attempts have been made to relaminarize a fully developed turbulent flow [16].

We will consider two fundamentally different stability scenarios for the evolution of perturbations  $q$  governed by the nonparallel Ginzburg–Landau equation: (i) local convective instabilities and (ii) global instabilities. The parameters for the two cases are listed in Table 1.

**5.1 The Concept of Feedback.** The actuation on the flow can be accomplished by various means, for example, the injection of fluid through blowing/suction holes in the wall. Within the region of validity of our underlying physical model, it is possible to compute a control strategy in advance that will retain the flow in a laminar state. This procedure is referred to as open-loop control. However, under the presence of uncertainty over the exact disturbance environment (or the validity of our physical model), open-loop control will fail. Instead, one can monitor the flow through measurements and adjust the actuation accordingly such that predefined objectives are met. A control setup of this type is known as closed-loop control. It uses feedback to establish a connection between the output from the system (i.e., the measurement signal) and the input to the system (i.e., the control signal). Under realistic conditions, we are faced with a wide range of unknown varia-

tions, such as modeling errors or sensor noise, and a feedback-type control system is required to efficiently compensate for these uncertainties.

The main idea of linear feedback control is shown in Fig. 1. The entire system is described in state-space form as follows:

$$\dot{q} = Aq + B_1w + B_2u \quad (68a)$$

$$z = C_1q + Du \quad (68b)$$

$$y = C_2q + g \quad (68c)$$

This set of equations is commonly referred to as the *plant*. The first equation (68a) describes the dynamics of our linear system captured in the system matrix  $A$  as external forces, modeled by  $B_1w$  and  $B_2u$ , are applied. We have decomposed the input into two terms with  $B_1w(t)$  describing the effect of external sources of excitations and  $B_2u(t)$  representing the control input. The variable  $z(t)$  given by the second equation (68b) represents the objective function as described below. The third equation (68c) describes a connection between the state  $q$  and the measurements  $y$ , where the additional term  $g$  accounts for noise contaminating the measurements. In general, the objective is to find a control signal  $u(t)$  such that the influence of the external disturbances  $w$  and  $g$  on the output  $z$  is minimized. The above set of equations (68) has been discretized using a Hermite collocation method as described in Appendix.

Our objective is to find a control signal  $u(t)$  such that the perturbation energy contained in the state variable  $q(t)$  is minimized. Furthermore, the energy input expended by the control must be smaller than the amount of energy gained by it. Thus, in addition to focusing on the perturbation energy, we also have to penalize our control effort. This results in an objective (or cost) functional of the form

$$\|z\|_2^2 = \|C_1q\|_2^2 + \|Du\|_2^2 = \int_0^T \underbrace{q^H C_1^H C_1 q}_M + \underbrace{u^H D^H D u}_R dt \quad (69)$$

where  $M$  and  $R$  are positive semidefinite matrices; we have furthermore assumed that  $D^H [C_1 \ D] = [0 \ I]$  in order to get zero cross terms [23]. It is important to realize that the 2-norm in the above expression is defined both over time and space. Note that if  $C_1$  is chosen as  $F$  in Eq. (18) then the kinetic energy of the disturbance will be minimized. In the above setup, we have assumed that the full-state  $q$  is known, but for realistic flow situations the complete instantaneous velocity field is not available for determining an appropriate feedback. We thus have to *estimate* the full-state vector resulting in an approximate state vector  $\hat{q}$ , reconstructed from the measurements  $y(t)$  via an estimation problem. A controller based on an estimated state vector is known as an output feedback controller or a compensator.

**5.2 The LQG Framework.** If we assume that the unknown disturbance noise  $w$  and the measurement noise  $g$  are given by white-noise stochastic processes with zero mean and respective covariances  $W$  and  $G$ , a compensator can be found that minimizes the cost functional (69). In addition, the closed-loop control is guaranteed to be stable, if the plant is both observable and controllable. In fact, a sufficient condition for a global minimum value of Eq. (69) is that the system is stabilizable and detectable. A system is stabilizable (detectable) if all unstable global modes are controllable (observable).

The control will be optimal in minimizing Eq. (69) which stems, in one part, from the optimal filtering of noise that has corrupted our signal [98] and, in another part, from the optimal control when the entire state vector is assumed to be available. These two separate problems—the estimation problem and the full-information problem—can then be combined to construct a

compensator. This two-step procedural framework matured in the 1960s into what we now refer to as LQG control [20,21]. The assumption that  $w(t)$  and  $g(t)$  are white-noise stochastic processes may be far from reality in some applications; it is, however, possible to describe a plant with colored-noise input in terms of an augmented system with white-noise input [22].

In applications, LQG control is particularly successful when the system operator  $A$  (in our case the Ginzburg–Landau equation) accurately describes the modeled physical phenomenon. The remaining uncertainties in the overall model are thus restricted to the inputs represented by stochastic disturbances with known statistical properties. For this reason, the LQG framework is appropriate when we can rely on an accurate plant, while a precise knowledge of external disturbances and the degree of noise contamination of the measurements are not available.

If the external disturbances are stochastic variables, the state will as well be a stochastic process, and the objective function (69) can therefore be written as

$$\|z\|_2^2 = \mathcal{E}\{q^H M q + u^H R u\} \quad (70)$$

As alluded to above, we will determine the optimal control  $u(t)$  in Eq. (68) based on noisy measurements  $y(t)$  such that the cost functional (70) is minimized. The first step in constructing such a compensator is to estimate the full-state  $q(t)$  given only the noisy measurements. After the state has been successfully estimated, we assume, in a second step, that the control  $u(t)$  and the estimate of the state  $\hat{q}(t)$  satisfy a linear relation involving some yet unknown matrix  $K$ , i.e.,

$$u(t) = K\hat{q}(t) \quad (71)$$

The goal of this second step is then to find such a matrix  $K$ , which is referred to as the control gain.

At the heart of the LQG-framework is the separation principle [80], which states that the controller that minimizes Eq. (69) can be computed in two independent steps: (i) we can solve the estimation problem to obtain an approximation  $\hat{q}$  of the true state  $q$  without any reference to the control problem; (ii) to find the control gain  $K$  in Eq. (71) we do not need the estimate  $\hat{q}$  in Eq. (71) but instead can assume the full-information relation  $u(t) = Kq(t)$ . One of the important consequences of the separation principle is the fact that the final compensator, using (71) based on the control gain  $K$  obtained by considering  $q(t)$  (not  $\hat{q}$ ), will always yield a closed-loop system that is stable if and only if each of the two separate problems (estimation and full-information control) are themselves stable (see Ref. [23]). In addition to stability, the closed-loop system will be optimal. To simplify the expressions in the following analysis, we assume that the adjoint system is derived using a standard Euclidean inner product, i.e., the dual or the adjoint of the plant (68) is given simply by its complex conjugate transpose.

**5.2.1 The Estimation Problem.** Under the assumption that the measurements capture a sufficient amount of the system's dynamics (i.e., that we have significant observability), it is possible to estimate or observe the state vector by using a Kalman filter [98]. In this section, we derive the algebraic Riccati equation for estimation and show examples on the Ginzburg–Landau equation. For additional details, see, e.g., Refs. [20,22].

We assume zero initial conditions, since we are interested in the controller performance as an average over long time while the system is excited by external perturbations. We further assume white-noise stochastic processes for  $w(t)$  and  $g(t)$  with zero mean. The estimator then takes on the form

$$\dot{\hat{q}} = A\hat{q} + B_2u - L(y - \hat{y}) \quad (72a)$$

$$\hat{y} = C_2 \hat{q} \quad (72b)$$

In the above expression, we compare the measurement  $y$  from the state and the measurement  $\hat{y}$  from the estimated state and feedback the mismatch in these two quantities using the estimator gain  $L$ . To analyze the performance of the estimation problem, it is instructive to derive the dynamics of the estimation error  $\tilde{q} = q - \hat{q}$ . Combining Eqs. (68) and (72), we obtain

$$\dot{\tilde{q}} = A\tilde{q} + B_1 w + L(y - \hat{y}) \quad (73)$$

Substituting the explicit dependence of the two measurements on the state  $q$  and estimated state  $\hat{q}$ , respectively, we obtain

$$\dot{\tilde{q}} = (A + LC_2)\tilde{q} + B_1 w + Lg \quad (74)$$

where the estimation error dynamics is governed by the matrix  $A_e = A + LC_2$  and is driven by two source terms, namely, the external excitation  $w$  and the sensor noise  $g$ . We aim at finding an estimator gain  $L$  such that  $A_e$  is asymptotically stable and is not sensitive to the external perturbations  $B_1 w + Lg$ . Since Eq. (68) is driven by noise, the state  $q(t)$  and the output  $y(t)$  are consequently random processes whose stochastic properties have to be considered in finding the estimator gain  $L$ . The error covariance is given as

$$P(t) = \mathcal{E}\{\tilde{q}\tilde{q}^H\} \quad (75)$$

which represents a measure of uncertainty in the estimate. Smaller values of  $P(t)$  indicate a better estimate as the estimation error is more tightly distributed about its mean value of zero. If the estimator (74) is stable, the error  $\tilde{q}(t)$  will eventually reach a steady state with a constant mean and covariance. The steady-state covariance can be readily obtained by solving the Lyapunov equation

$$A_e P + PA_e^H + LGL^H + B_1 WB_1^H = 0 \quad (76)$$

where  $G$  and  $W$  are the covariance matrices of  $g(t)$  and  $w(t)$ , respectively. The optimal estimation feedback gain  $L$  is then chosen to both keep Eq. (74) stable and to minimize the mean of the steady-state estimation error. We obtain the mean estimation error from the covariance (75) using the expression (38),

$$J = \mathcal{E}\{\tilde{q}\} = \text{tr}(PM) \quad (77)$$

where the mean is chosen as the kinetic energy. This minimization has to be accomplished under the constraint that  $P$  satisfies the above Lyapunov equation (76). We add this constraint to the cost functional  $J$  via a Lagrange multiplier  $\Lambda$  and obtain the Lagrangian  $\mathcal{M}$ :

$$\mathcal{M} = \text{tr}(PM) + \text{tr}[\Lambda(A_e P + PA_e^H + LGL^H + B_1 WB_1^H)]$$

We thus minimize  $J$  subject to the constraint (76) by equivalently finding stationary points of  $\mathcal{M}$  without imposed constraints. The necessary conditions for a minimum are given by

$$\frac{\partial \mathcal{M}}{\partial P} = A_e^H \Lambda + \Lambda^H A_e + M = 0 \quad (78a)$$

$$\frac{\partial \mathcal{M}}{\partial \Lambda} = A_e P + PA_e^H + LGL^H + B_1 WB_1^H = 0 \quad (78b)$$

$$\frac{\partial \mathcal{M}}{\partial L} = 2\Lambda(P C_2^H + LG) = 0 \quad (78c)$$

We can eliminate  $\Lambda$  from Eq. (78c) to obtain an expression for the estimator gain

$$L = -PC_2^H G^{-1} \quad (79)$$

Inserting the expression above into the second condition (78b) leads to a quadratic matrix equation for the error covariance  $P$ :

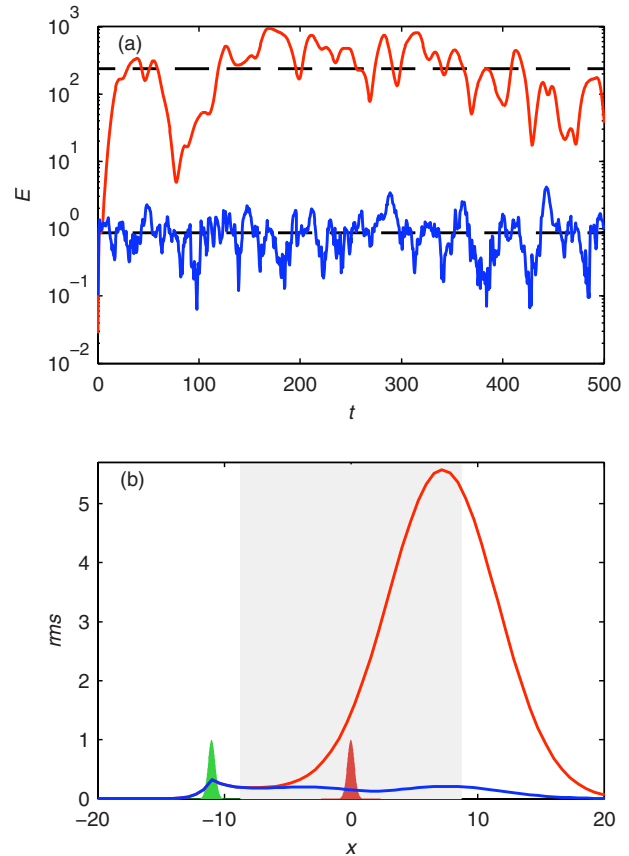


**Fig. 25 (a)** The mean of the error covariance  $\text{tr}(PM)$  (lower dashed line) obtained by solving the Riccati equation (80) is compared to the estimation error (blue line) obtained by marching the estimator in time (72). Also, the mean value of the state (top dashed line/red line) is shown and found to be nearly three orders of magnitude larger than the estimation error. It is evident that both the state and the estimation error reach a steady state. **(b)** The rms value of the error and the state are shown in blue and red lines, respectively. The red and green Gaussian functions represent the location of the input (stochastic disturbances) and the sensor. The error attains its minimum value just downstream of the sensor location and increases upstream and downstream of it.

$$AP + PA^H - PC_2^H G^{-1} C_2 P + B_1 WB_1^H = 0 \quad (80)$$

which is referred to as an algebraic Riccati equation. In Refs. [74,99], efficient methods of solving the Riccati equations can be found. We can thus determine the optimal estimation gain  $L$  by solving Eq. (80) for the error covariance  $P$  which, using Eq. (79), results in  $L$ . No requirements of observability or controllability have to be explicitly imposed on the estimation problem; however, if we place the input describing external disturbances  $B_1$  and the sensor  $C_2$  such that  $(C_2, A)$  is observable and  $(A, B_1)$  is controllable, then the resulting Riccati equation (80) will have a unique positive-definite solution. Moreover, the closed-loop estimator will then be asymptotically stable.

One way to investigate the performance of the estimator is to compare the energy of the true flow state with the energy of the estimation error. In Fig. 25(a), the temporal evolution of the state energy (red line) and of the estimation error (blue line) are shown. The energy of the estimation error is nearly three orders of magnitude smaller than the energy of the true state. In the same figure, the mean energy of the estimation error—obtained by solving the Riccati equation (80)—and the mean energy of the state—obtained by solving the Lyapunov equation (44)—are plotted with dashed lines. We observe that the solutions of the Riccati equation

and the Lyapunov equation provide the mean energy in which, respectively, the estimation error and state energy fluctuate about. In Fig. 25(b), the corresponding rms of the error  $\tilde{q}_{\text{rms}}$  together with the rms of state  $q_{\text{rms}}$  are shown.

**5.2.2 Full-Information Control.** The second step in the design of a LQG compensator involves the solution of an optimal control state-feedback problem. We show in this section that the optimal solution is again provided by the solution of a Riccati equation. The reader is directed to Refs. [20,22] for more detailed derivations.

We seek a control  $u(t)$  as a linear function of the flow state  $q(t)$  that minimizes the deterministic cost functional

$$J = \frac{1}{2} \int_0^T q^H M q + u^H R u dt, \quad M, R > 0 \quad (81)$$

while satisfying the initial value problem

$$\dot{q} = Aq + B_2 u, \quad q(t=0) = q_0 \quad (82)$$

We perform the steps analogous to the estimation problem by first defining an augmented Lagrangian  $\mathcal{N}$  of the form (see Ref. [22])

$$\mathcal{N} = \frac{1}{2} \int_0^T (q^H M q + u^H R u) + \lambda^T (-\dot{q} + Aq + B_2 u) dt \quad (83)$$

where  $\lambda$  is again a Lagrange multiplier, which enforces the initial value problem (82). The necessary conditions for a minimum of  $\mathcal{N}$  result in the following set of equations

$$\frac{\partial \mathcal{N}}{\partial \lambda} = -\dot{q} + Aq + B_2 u = 0 \quad (84a)$$

$$\frac{\partial \mathcal{N}}{\partial q} = \dot{\lambda} + Mq + A^H \lambda = 0 \quad (84b)$$

$$\frac{\partial \mathcal{N}}{\partial u} = Ru + B_2^H \lambda = 0 \quad (84c)$$

We proceed by assuming a linear relation between the state  $q(t)$  and the Lagrange multiplier  $\lambda(t)$ :

$$\lambda(t) = X(t)q(t) \quad (85)$$

where  $X(t)$  is self-adjoint and positive semidefinite. Using this linear relation and the optimality condition (84c) yields the following feedback law:

$$u(t) = \underbrace{-R^{-1}B_2^H X(t)}_{K(t)} q(t) \quad (86)$$

To find  $X(t)$ , we differentiate (85) and use the state equation (84a) to obtain

$$-\dot{\lambda} = \dot{X}q + X(Aq - B_2^H R^{-1} B_2 X q) \quad (87)$$

Substituting Eq. (84b) into this last expression leads to a quadratic matrix equation for  $X(t)$  that (assuming controllability of  $(A, B_2)$ ) asymptotically converges to

$$A^H X + X A - X B_2 R^{-1} B_2^H X + M = 0 \quad (88)$$

As before, we obtain a Riccati equation for the linear mapping  $X$ . The solution to this equation provides the optimal steady feedback gain via the relation (86).

Moreover, stabilizability of  $(A, B_2)$  and detectability of  $(A, C_1)$  imply additional desirable properties: The feedback gain  $K$  is guaranteed to stabilize the plant and to yield a global minimum value of Eq. (81). We recall that a system is stabilizable (detectable) if all unstable global modes are controllable (observable). In

other words, if we place our actuators such that we ensure controllability of the unstable global modes and if we choose  $M$  as the kinetic energy weight matrix, then the closed-loop system is guaranteed to be stable. In the limit as  $T \rightarrow \infty$ , the cost functional is given by (see Ref. [100])

$$J = q_0^H X q_0 \quad (89)$$

and any other stabilizing controller will result in a larger value of this objective functional.

**5.2.3 The LQG Compensator.** Combining the estimator and controller, we can now control our plant by solely relying on the measurements  $y(t)$ . To validate the separation principle, we may write the control (71) in terms of the full-state  $q$  and the estimation error  $\tilde{q}$ ,

$$u = Kq - K\tilde{q} \quad (90)$$

We can combine the plant (68) and the equation for the estimation error (74) into the augmented system

$$\begin{pmatrix} \dot{q} \\ \dot{\tilde{q}} \end{pmatrix} = \begin{pmatrix} A + B_2 K & -B_2 K \\ 0 & A + LC_2 \end{pmatrix} \begin{pmatrix} q \\ \tilde{q} \end{pmatrix} + \begin{pmatrix} B_1 & 0 \\ B_1 & L \end{pmatrix} \begin{pmatrix} w \\ g \end{pmatrix} \quad (91)$$

Since this augmented system is block triangular, the eigenvalues of the augmented closed-loop system consist of the union of the eigenvalues of  $A_c = A + B_2 K$  and  $A_e = A + LC_2$ . Thus, if the full-information controller  $A_c$  and the estimator  $A_e$  are stable, then the closed-loop system, i.e., the compensator, obtained by combining the plant (68) and estimator (72),

$$\begin{pmatrix} \dot{q} \\ \dot{\tilde{q}} \end{pmatrix} = \underbrace{\begin{pmatrix} A & B_2 K \\ -LC_2 & A + B_2 K + LC_2 \end{pmatrix}}_A \begin{pmatrix} q \\ \tilde{q} \end{pmatrix} + \underbrace{\begin{pmatrix} B_1 & 0 \\ 0 & -L \end{pmatrix}}_B \begin{pmatrix} w \\ g \end{pmatrix} \quad (92a)$$

$$z = \underbrace{(C_1 \quad DK)}_C \begin{pmatrix} q \\ \tilde{q} \end{pmatrix} \quad (92b)$$

is also stable. As the separation principle suggests, the compensator consisting of an optimal estimator and an optimal full-state controller is itself optimal. The closed-loop system, given by Eq. (92), has two inputs, the external disturbances  $w$  and the measurements noise  $g$ , and one output, the objective function  $z$ . This closed-loop system is treated as a new dynamical system whose properties, such as stability, input-output behavior and performance, have to be investigated. Next, we discuss these issues for the two prototypical flow cases.

**5.3 Control of Subcritical Flow.** For a choice of parameters that results in a convectively unstable plant (Table 1), the objective is to apply control schemes that lower transient energy growth or reduce the amplification of external disturbances. We will now construct a LQG compensator for the Ginzburg–Landau equation to illustrate how a typical convectively unstable flow system may react to control. Similar to the analysis of the uncontrolled system in Secs. 2 and 3, the response behavior of the closed-loop system—in terms of spatiotemporal evolution of the state, kinetic energy, and sensor signal—will be investigated for various inputs, optimal initial disturbance, harmonic forcing, and stochastic forcing.

Before control schemes can be designed, one has to decide on the placement of actuators and sensors, the choice of which is reflected in the matrices  $B_2$  and  $C_2$ . We assume the spatial distribution of the inputs and the outputs as Gaussian functions of the form given by Eq. (A4). The width parameter  $s=0.4$  is chosen such that 95% of the spatial extent of the input/output distributions are ~5% of the length of the unstable domain (see Fig. 26(a)). In this way, we are restricted—as in any practical implementation of control schemes—to only a limited number of noisy

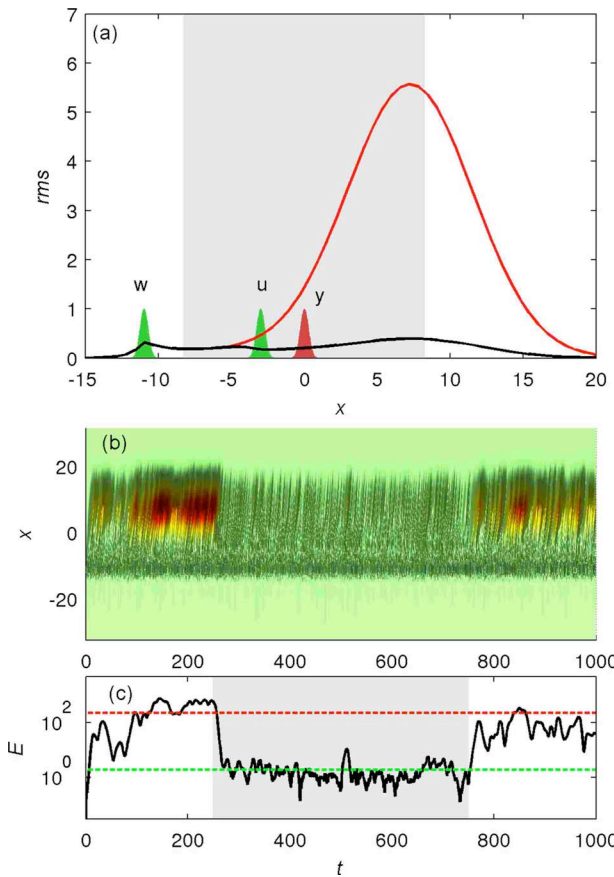


**Fig. 26 The controlled Ginzburg–Landau equation with stochastic excitation:** (a) White noise  $w$  with zero mean and unit variance  $W=1$  forces the system at  $x=-11$ , just upstream of unstable region with input  $B_1$  as a Gaussian function (green). Measurements  $y(t)$  of the state (red Gaussian) contaminated by white noise with zero mean and variance  $G=0.1$  are taken at  $x_s=0$ . The actuator  $u$  with control penalty  $R=1$  is placed upstream of the sensor at  $x_u=-3$ . The rms values of the uncontrolled and LQG-controlled state are given by the solid red and black lines, respectively. The absolute value of the state  $|q|$  is shown in an  $x$ - $t$ -plane in (b), while the lower plot (c) displays the kinetic energy  $E=\|q\|_M^2$  as a function of time. The control is only engaged for  $t \in [250, 750]$ . Dashed lines in (c) indicate the mean value computed from Lyapunov equation.

measurements and to actuation in a rather small region of the full domain. An additional simplification is made by considering only one actuator and one sensor.

Identifying regions of the flow where sensing and actuation are favorable to the feedback control of a convectively unstable system is significantly complicated by the convective nature of the flow. Usually one has to use physical intuition and a trial-and-error approach. Transient growth of energy due to the non-normality of  $A$  is associated with the local exponential growth of disturbances between branches I and II. As a consequence—and in contrast to the globally unstable case (see Sec. 5.4), where it suffices to estimate at branch II and control at branch I—the entire unstable domain between branches I and II is of great importance for the flow dynamics.

Appropriate choices for the location of an actuator and a sensor for the subcritical Ginzburg–Landau equation is found to be  $x_u = -3$  and  $x_s = 0$ , respectively. In Fig. 26(a), the actuator and sensor placement are shown that result in an acceptable closed-loop performance.

**5.3.1 Stochastic Disturbance.** Consider a system driven by white noise  $B_1 w(t)$  just upstream of branch I. From the noisy measurements  $y(t) = C_2 q(t) + g$  between branches I and II, an estimated state is obtained. Based on this estimate, the control signal  $B_2 u(t)$  is applied upstream to the sensor. The placement of the excitation, sensor, and actuator is shown in Fig. 26(a).

The covariance of the external and measurement noise should be chosen to match as closely as possible the uncertainties that are expected for the chosen design configuration, but it is difficult to make more specific statements. It has, however, been found (see Refs. [13,66,73]) that the performance of the estimator can be improved dramatically if the covariances are chosen to reflect physically relevant flow structures rather than generic probability distributions. For our problem, the sensor noise  $g$  is chosen to have a variance of  $G=0.1$ , which is 10% of the variance of a random input with  $W=1$ .

Since Eq. (68) is driven by white noise  $w(t)$ , the state  $q(t)$  is consequently a random process and is defined by its stochastic properties, e.g., its covariance  $P = \mathcal{E}\{qq^H\}$ . As we have shown in Sec. 3.2, these properties are linked to the statistical characteristics of the forcing via a Lyapunov equation (44).

In Fig. 26(a), the rms values (39) of the state without control (red) and with control (black) are shown. The rms value of the uncontrolled state grows exponentially as it enters the unstable domain at branch I; this growth prevails until branch II. The rms of the controlled state, however, grows only slightly in the unstable region and is considerably lower than the rms value of the uncontrolled state at branch II.

In Figs. 26(b) and 26(c), the performance of the compensator is shown more explicitly in form of a temporal simulation of the closed-loop system (92) in time. The control is only engaged for  $t \in [250, 750]$ . Without control the stochastic disturbances grow exponentially as they enter the unstable region at  $x=-8.2$  and decay as they exit the region at  $x=8.2$ . When the control is activated, the perturbation energy is reduced from  $E \approx 10^3$  to  $E \approx 1$ . When the control is disengaged, the disturbances immediately start to grow again. During and after the time when the control is applied, the perturbation energy reaches a steady state at a level that can be determined from the covariance of the state according to  $E = \text{tr}(PM)$  (Eq. (38)). Dashed lines in Fig. 26(c) indicate these levels.

**5.3.2 Harmonic and Optimal Disturbance.** The aim of feedback control for subcritical flows is to design closed-loop systems with small transfer function norms compared to the stable open-loop system. Maximum transient energy growth of a perturbation and the norm of the system transfer function  $G$  are linked for highly non-normal systems (see Sec. 3.1 for details). To show this link, we will pose the LQG problem as a control problem in the frequency domain with the objective to minimize the 2-norm of the closed-loop transfer function.

The relation between the input and output signals, that is, between disturbance and measurement noise and the objective function,  $(w \rightarrow z, g \rightarrow z)$ , of the closed-loop system (92) (displayed schematically in Fig. 1) can be described by the transfer function

$$G_c(s) = \mathbf{C}(sI - \mathbf{A})^{-1} \mathbf{B}, \quad s \in \mathbb{C} \quad (93)$$

The relation between the objective function (69) in the time domain and in the frequency domain can easily be found from Parseval's identity,

$$\int_{-\infty}^{\infty} z^2 dt = \frac{1}{2\pi} \int_{-\infty}^{\infty} \text{tr}[G_c(i\omega)]_2^2 d\omega = \|G_c(i\omega)\|_2^2 \quad (94)$$

with  $|G_c|_2^2 = G_c^H G_c$ . We have thus defined the 2-norm of the transfer function  $G_c(s)$  as the integral over the 2-norm of the amplitude of the transfer function along the imaginary axis. The  $\mathcal{H}_2$  problem is then to minimize Eq. (94). The symbol  $\mathcal{H}_2$  stands for the “Hardy

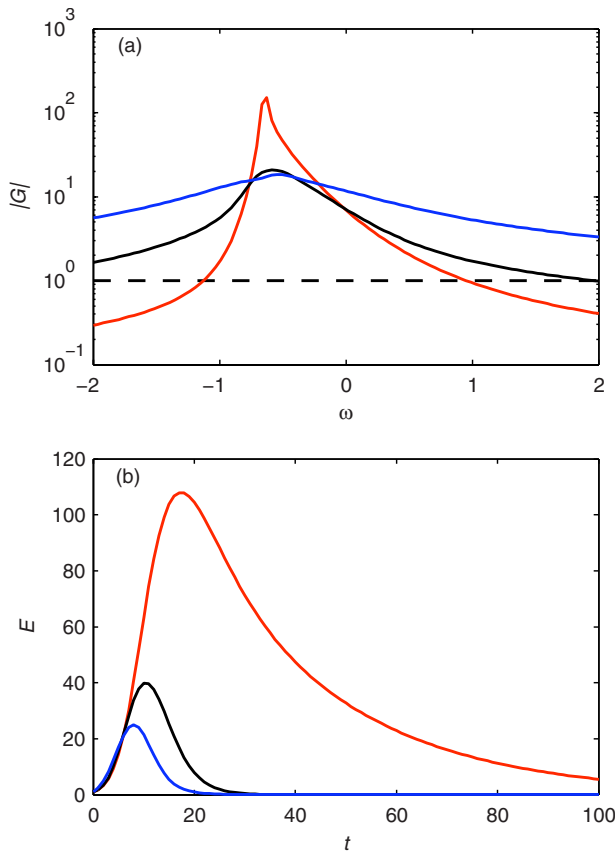


**Fig. 27 (a)** Comparison of the frequency response of the open-loop (red), LQG-controlled (black), and  $\mathcal{H}_\infty$ -controlled (blue) Ginzburg–Landau equations. For the open loop, the  $\infty$ -norm corresponding to the peak value of the response is 151, whereas the 2-norm corresponding to the integral of the response is 20.5. The  $\mathcal{H}_\infty$ -controller minimizes the peak value to 18.4 and reduces the 2-norm to 8.7. The LQG/ $\mathcal{H}_2$ -controller, on the other hand, minimizes the 2-norm to 6.1 and reduces the peak value to 20.8. (b) The energy evolution of an optimal disturbance is shown for the convectively unstable Ginzburg–Landau equation (red line) and the closed-loop system computed with LQG/ $\mathcal{H}_2$  (black) and  $\mathcal{H}_\infty$  (blue).

space” [23], which contains the set of stable transfer functions with bounded 2-norms.

In Fig. 27(a), the frequency response ( $w \rightarrow z, g \rightarrow z$ ) of the open-loop system is shown (red line) for the subcritical Ginzburg–Landau equation; we observe a 2-norm of 20.5. The corresponding LQG/ $\mathcal{H}_2$  closed-loop transfer function (93) is displayed (black line) in Fig. 27, where the 2-norm is now minimized to a value of  $\|G_c\|_2 = 6.1$ . In Fig. 27(b), the optimal energy growths (Sec. 2.3) of the uncontrolled and controlled system are compared. The maximum transient energy growth (peak value) is reduced by an order of magnitude.

**5.4 Control of Supercritical Flow.** For a globally unstable flow (parameters given in Table 1), i.e., an unstable plant (68), the influence of uncertainties ( $w(t)$  and  $g(t)$ ) on the system dynamics is rather small compared to the asymptotic behavior of the most unstable global mode. This mode will grow exponentially as soon as any disturbance (assuming it is not orthogonal to the unstable mode) enters the unstable region. For this reason, disturbance modeling may not play a decisive role for globally unstable flows, in contrast to convectively unstable flows.

The goal of any control effort is to stabilize an otherwise unstable system; this task is particularly straightforward using LQG-

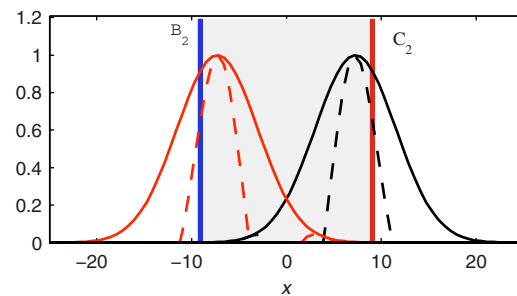


**Fig. 28** Actuator and sensor placement for the supercritical Ginzburg–Landau equation, which yields a stabilizable and detectable system. The spatial support of the actuator (blue bar), sensor (red bar), the unstable domain (gray region), and the unstable global mode (black lines) together with its corresponding adjoint mode (red lines) are shown.

based feedback control, since the closed-loop system (92) is guaranteed to be stable as long as the actuator and the sensor are placed such that the system is both stabilizable and detectable.

In other words, the performance of a controller to a globally unstable Ginzburg–Landau equation can only be successful if all unstable global modes are controllable and observable. It was concluded in Sec. 4.1 that a global mode is controllable (observable) if the overlap of the actuator (sensor) and the adjoint mode (global modes) is nonzero. In Fig. 28, a configuration for the actuator and sensor is shown that yields a plant, which is both stabilizable and detectable.

For this setup, a LQG compensator (92) is constructed by solving the Riccati equations (88) and (80). The perturbation energy, the impulse response, and the spectrum of the uncontrolled plant (68) and controlled closed-loop system (92) are shown in Figs. 29 and 30. We observe that the closed-loop system has all eigenval-

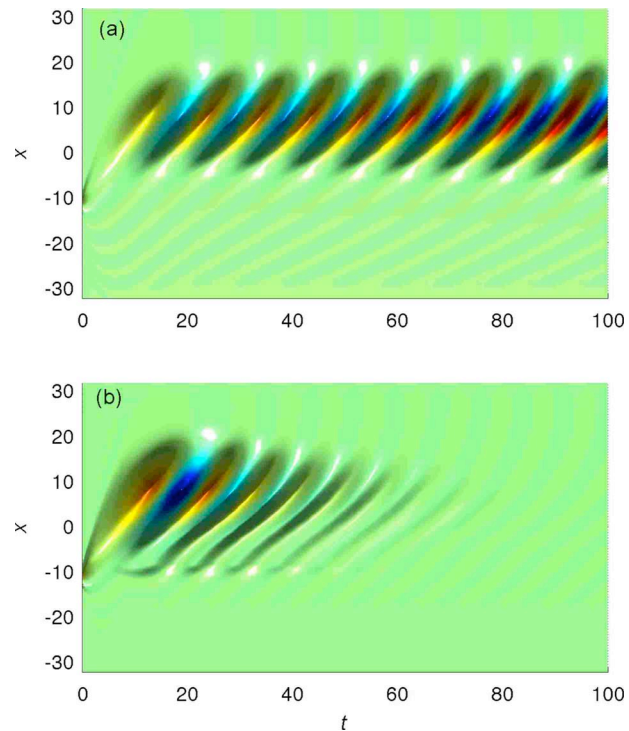


**Fig. 29** The spatiotemporal response to an impulse in time induced at  $x = -10$  for the uncontrolled system (a) and LQG-controlled system (b).

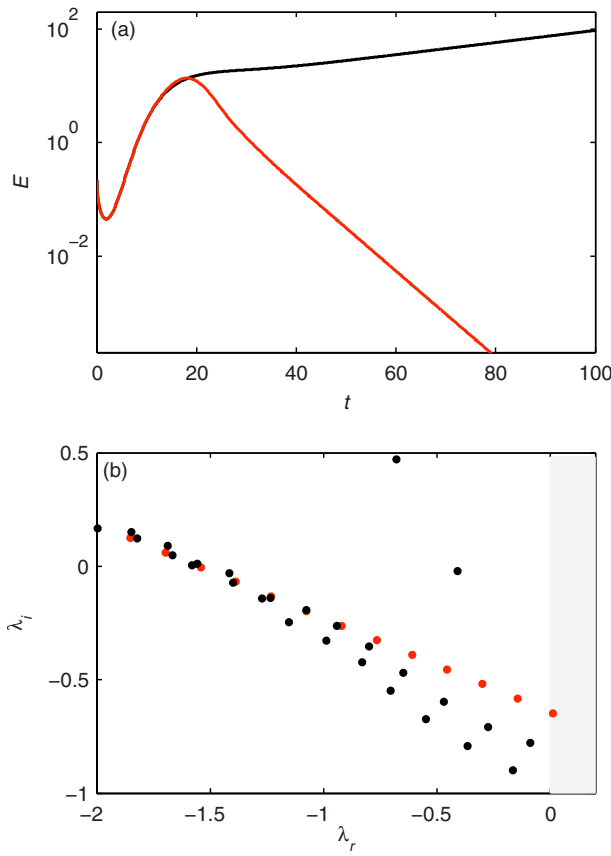


**Fig. 30 (Top)** The perturbation energy of an initial condition, which illustrates the asymptotic growth and the decay of the global mode of the controlled and uncontrolled systems. **(Bottom)** The spectrum of the uncontrolled (red) and LQG-controlled (black) Ginzburg–Landau equations. The exponential growth of the wavepacket in Fig. 29(a) is due to one unstable global mode of the open loop shown by the red circle in the unstable half-plane (gray region). The LQG-based closed loop is stable with no unstable eigenvalues.

ues in the stable half-plane yielding an asymptotically stable flow.

For a pointwise spatial distribution of actuators  $\delta(x-x_a)$ , it has been shown in Ref. [33] that the Ginzburg–Landau equation gradually loses stabilizability as the parameter  $\mu_0$  is increased. This loss is due to the increasing number of unstable global modes which are located further downstream. Controllability of the unstable global modes is gradually diminished as the support of the actuator and the support of the corresponding unstable adjoint global modes (56c) move apart until controllability is entirely lost. At this point no compensator will be able to stabilize the system using one pointwise actuator.

**5.5 The  $\mathcal{H}_\infty$  Framework: Robust Control.** In Secs. 2–4, we have tacitly assumed that the system matrices  $A$ ,  $B$ , and  $C$  are known exactly. In reality, however, this is not the case, since modeling errors (for example, a small mismatch in the Reynolds number between the model and the actual flow) are always present. The presence of these errors raises the important issue of robustness of a specific control design.

Concentrating for simplicity on the dynamic model error, let us consider a model system given by  $A$ . The real flow, on the other hand, shall be subjected to a small deviation from this model and is described by the dynamic matrix  $A + \epsilon\Delta$  with  $\Delta$  as a unit-norm uncertainty matrix and with  $\epsilon$  parametrizing the magnitude of the uncertainty. For a given value of  $\epsilon$ , the controller designed for  $A$  has the “robust stability” property if the closed-loop system is stable for all unit-norm uncertainty matrices  $\Delta$  and, similarly, has

the “robust performance” property if the performance of the closed-loop system is satisfactory for all possible unit-norm uncertainty matrices  $\Delta$ . If information about the specific form of the uncertainties is available, one can restrict the structure of the uncertainty matrix  $\Delta$  to reflect this information and thus reduce the “uncertainty set.” In a similar fashion, the magnitude  $\epsilon$  of the uncertainty may be estimated or bounded.

Unfortunately, the LQG/ $\mathcal{H}_2$ -control design does not account explicitly for uncertainties in the system matrices, which is needed to guarantee robust performance or even robust stability. For a given controller, the smallest value of  $\epsilon$  such that the closed-loop system is unstable is referred to as the *stability margin*. It is known [101] that there are no guaranteed stability margins for LQG/ $\mathcal{H}_2$ -controllers. However, this does not necessarily mean that the  $\mathcal{H}_2$ -controller will be unstable for very small values of  $\epsilon$ ; instead, it merely means that the search for robustness is not accounted for.

To incorporate the presence of uncertainties into the control design framework, one can adjust the actuation penalty and sensor noise, which, in turn, directly affects the strength of the controller and may help push the control design toward robustness. This approach has led to the development of control optimization based on the  $\mathcal{H}_\infty$ -norm. Instead of minimizing the energy of the transfer function (i.e., the integral of the frequency response over all frequencies), it concentrates instead on reducing the peak value of the frequency response. These are two very different objectives: for instance, a strong peak in the frequency response localized about one single frequency may not contribute significantly to the energy (integral) of the response. This new  $\mathcal{H}_\infty$ -objective plays a pivotal role in the search for robustness since closed-loop instabilities can be quantified by the relation between the magnitude of the dynamic uncertainty and the maximum frequency response (see Ref. [23]).

The steps to compute  $\mathcal{H}_\infty$ -controllers closely follow the ones for LQG/ $\mathcal{H}_2$ -design except that a new term is added to the objective functional that will represent the worst possible external forcing. The subsequent optimization scheme will search for a controller that achieves the best performance for the worst perturbation (see Refs. [11,24]). Mathematically, this is equivalent to searching for a saddle point of this new objective functional rather than a minimum. The augmented objective functional reads

$$J = \int_0^T q^H M q + u^H R u - \gamma^2 w^H W w dt \quad (95)$$

In this expression,  $w$  represents both external disturbances and measurement noise. We then wish to find the control  $u$ , which minimizes the control objective (69) in the presence of a disturbance  $w$  that maximally disrupts this objective. A new free parameter  $\gamma$  appears that plays the role of  $\epsilon$  in parametrizing the magnitude of the worst perturbation.

To simplify the following derivation, we assume for now that  $W=1$  and  $R=1$ . Similar to the LQG design in Sec. 5.3.2, we can also specify the control objective in the frequency domain instead of the time domain (95). In this case, we simply aim at restricting the maximum values of the closed-loop transfer function as given by (see, e.g., Ref. [79])

$$\|G_c(i\omega)\|_\infty \leq \frac{\|z\|_2}{\|w\|_2} \leq \gamma \quad (96)$$

The above transfer function norm was defined in Eq. (35).

The  $\mathcal{H}_\infty$ -problem consists of finding a control signal  $u(t)$  that minimizes both the perturbation energy and control effort while maximizing the effects of the external disturbances  $w$ . As the parameter  $\gamma$  approaches infinity, the objective functional (and the optimal control) reduces to the one of the LQG problem. In this review, we will merely present the solution of the  $\mathcal{H}_\infty$ -problem

and show how it relates to the LQG-solution. For a more detailed derivation of this link, see Ref. [23] or Ref. [79].

The solution of the above  $\mathcal{H}_\infty$ -problem is, similar to the LQG-problem, obtained by solving two Riccati equations, which stem from two separate problems: the estimation and the full-information control problem. The full-information control problem leads to the Riccati equation of the form

$$A^H X + X A - X(-\gamma^{-2} B_1 B_1^H + B_2 B_2^H)X + M = 0 \quad (97)$$

with the control given by

$$u = -\underbrace{B_2^H X q}_{K} \quad (98)$$

Furthermore, one finds that the worst-case disturbance  $w$  is given by

$$w_{\text{worst}} = \gamma^{-2} B_1^H X q \quad (99)$$

The Riccati equation (97), whose solution yields the control feedback gain for  $\mathcal{H}_\infty$ , is modified such that it takes into account the worst-case disturbance acting on the system. We notice that the term  $-\gamma^{-2} B_1 B_1^H$  is absent in the Riccati equation (88) of the LQG problem. Rather, by modeling and incorporating the structure of the disturbances  $B_1$  when computing the feedback gain  $K$ , the components of the state that are expected to be most influenced by external disturbances are forced by the largest feedback,  $K\hat{q}$ . We would like to point out that the parameter  $\gamma$  is supplied by the user and that the resulting control (98) is only suboptimal rather than optimal. For large values of  $\gamma$ , the full-information solution of the associated LQG problem and the optimal control signal are recovered.

The estimated state is also computed in the presence of worst-case disturbances  $\hat{w}_{\text{worst}} = \gamma^{-2} B_1^H X \hat{q}$  and is therefore the result of the following estimation problem:

$$\dot{\hat{q}} = A\hat{q} + B_1 \hat{w}_{\text{worst}} + B_2 u - L(y - \hat{y}) \quad (100a)$$

$$\hat{y} = C_2 \hat{q} \quad (100b)$$

Similar to the LQG-estimation problem, the difference between the true measurement  $y$  and the estimated measurement  $\hat{y}$  is fed back using the estimator gain  $L$ . There is, however, no longer any assumption on the disturbances  $w$  and  $g$ . Instead the additional term  $B_1 \hat{w}_{\text{worst}}$  provides the estimator with information on the worst-case disturbance. The estimation gain in Eq. (100) is given by  $L = -ZYC_2^H$ , where  $Y$  is the solution of the following Riccati equation (for a derivation of this result see, e.g., Ref. [23])

$$AY + YA^H - Y(-\gamma^{-2} C_1^H C_1 + C_2^H G^{-1} C_2)Y + B_1 B_1^H = 0 \quad (101)$$

and  $Z$  is a constant matrix given by

$$Z = (I - \gamma^{-2} Y X)^{-1} \quad (102)$$

Equation (101) can now be compared to the Riccati equation (80) for the LQG problem. The additional term  $-\gamma^{-2} C_1^H C_1$  is present in the above equation, which reflects the fact that the computation of the estimation gain  $L$  depends on the weights in the cost functional. The components of the estimated state that most contribute to the objective functional are forced stronger by the feedback  $L(y - \hat{y})$ . In addition, we notice that the estimation gain  $L$  depends via Eq. (102) on the solution of the full-state Riccati solution  $X$ .

By combining the estimator (100) and the plant (68), it is straightforward to formulate the  $\mathcal{H}_\infty$ -compensator as a closed-loop system. Even though the required calculations (the solution of two Riccati equations) are reminiscent of the LQG approach, in the  $\mathcal{H}_\infty$  case we face additional restrictions for the stability of the closed-loop system and a more demanding computational effort for finding an optimal controller.

First, stabilizability and detectability are no longer a sufficient condition to guarantee the stability of the closed-loop system. For the  $\mathcal{H}_\infty$ -problem to be solvable, the spectral radius  $\rho$  of  $XY$  has to be smaller than  $\gamma^2$  (see Ref. [102]).

Second, the solution presented above is merely suboptimal; finding an optimal robust controller involves an iterative process that terminates when a lower bound  $\gamma_0$  of  $\gamma$  is found, which still satisfies  $\rho(XY) < \gamma^2$ . This optimal  $\gamma_0$  can typically be found with fewer than 20 iterations using the bisection algorithm.

We use the Ginzburg–Landau equation to exemplify the techniques introduced above. For a more detailed investigation, we refer to Ref. [34]. In Fig. 27(a), the frequency response (i.e., the mapping  $w, g \rightarrow z$ ) of the open-loop system is shown with a red line for the subcritical Ginzburg–Landau equation, displaying an  $\infty$ -norm of 151. The corresponding  $\mathcal{H}_\infty$  closed-loop design is shown with a blue line where the  $\infty$ -norm is now reduced to  $\|G_c\|_\infty = 18.4$ . Comparing the frequency responses of the controlled systems based on the  $\mathcal{H}_2$  and  $\mathcal{H}_\infty$ , we can confirm that in the former case the 2-norm  $\|G_c\|_2$  is minimized while in the latter case  $\|G_c\|_\infty$  is minimized. Consequently, the most amplified frequencies are more damped in the  $\mathcal{H}_\infty$ -case at the expense of the higher frequencies, which are amplified compared to the uncontrolled case. The  $\mathcal{H}_2$ -controller, on the other hand, shows a smaller reduction in the most unstable open-loop frequencies (i.e., the peak value in the frequency response). This is not surprising, since the  $\mathcal{H}_2$ -controller minimizes the energy—the integral of the transfer function along the imaginary axis—whereas the  $\mathcal{H}_\infty$ -controller minimizes the peak value of the transfer function on the imaginary axis.

The optimal energy growth (see Eq. (20)) in Fig. 27(b) demonstrates that the maximum energy growth is smaller for the  $\mathcal{H}_\infty$ -design, which suggests that reducing the most amplified frequencies, rather than all the frequencies, is a more efficient strategy for damping maximum energy growth. However, to achieve its goal the  $\mathcal{H}_\infty$ -controller expends more control energy than the corresponding  $\mathcal{H}_2$ -controller [34].

Using the Ginzburg–Landau equation for a set of parameters that yields a globally unstable flow, Lauga and Bewley [34] compared the  $\mathcal{H}_\infty$ -controller to the  $\mathcal{H}_2$ -controller for a range of control penalties and various levels of measurement noise. They found that the  $\mathcal{H}_\infty$ -control design always uses more control energy (for the same control penalty) than the corresponding  $\mathcal{H}_2$ -control design. A robust controller uses this additional control energy to ensure that the constraint on the maximum value of the transfer function norm  $\|G_c\|_\infty$  is satisfied.

**5.6 Reduced-Order Controllers.** The process of systematic control design as presented above involves the solution of two Riccati equations. The cost of computing a Riccati solution is of order  $n^3$ , where  $n$  is the number of components in the discretized state vector. Whereas for the Ginzburg–Landau equation  $n$  is still sufficiently low to allow a direct solution of the Riccati equations, for the Navier–Stokes equations the number of state vector components is rather large. The cost of a direct Riccati solution is prohibitively expensive when  $n > 10^5$ , which is easily reached for two- and three-dimensional flow configurations. As discussed in Sec. 4, this high cost can be avoided by developing a reduced-order model, which preserves the essential flow dynamics.

Similar to solving a Lyapunov equation, there exist “matrix-free” methods to solve a Riccati equation. One common approach that significantly reduces the cost of directly solving the Riccati equation—if the number of inputs and outputs is much smaller than the number of states—is known as the Chandrasekhar method [103]. In this method, the Riccati solution is expressed as the solution to a coupled system of ordinary differential equations, which needs to be integrated in time (see Ref. [66] for an application).

Even if we manage to obtain the feedback gains from the full system, however, there still remains the issue that the controller is of very high order, which requires a rather fast feedback system running next to the experiment.

We will return to the issue of model reduction (see Sec. 4) based on the projection of the original high-dimensional system onto a smaller system using a given basis. One of the main advantages of this approach is that the error in the reduced-order model can be quantified in terms of transfer functions, as shown in Eqs. (61) and (57).

Once a reduced-order model is devised (using the techniques in Sec. 4) whose transfer function is a sufficiently good approximation of the open-loop transfer function, we can design an  $\mathcal{H}_2$ - or an  $\mathcal{H}_\infty$ -controller for this reduced model. This results in a reduced-order controller, which, coupled to the full-order open-loop system, will result in the following augmented system:

$$\begin{pmatrix} \dot{\hat{q}} \\ \dot{\hat{q}} \end{pmatrix} = \begin{pmatrix} A & B_2 \hat{K} \\ -L \hat{C} & \hat{A} + \hat{B}_2 \hat{K} + \hat{L} \hat{C} \end{pmatrix} \begin{pmatrix} q \\ \hat{q} \end{pmatrix} + \begin{pmatrix} B_1 & 0 \\ 0 & -\hat{L} \end{pmatrix} \begin{pmatrix} w \\ g \end{pmatrix} \quad (103)$$

The expression of the reduced-order controller is similar to the full order given by Eq. (92), except that the quantities marked with “ $\hat{\cdot}$ ” are of order  $r \ll n$ . Note that the feedback gain  $K$  and estimation gain  $L$  have the dimension of the reduced model resulting in a fast online controller.

We can now compare the frequency response of the reduced-order models with and without control. The frequency response of the full model without control was shown by the dashed blue lines in Fig. 22. The frequency response of reduced-order models using global modes (green), POD modes (black), and balanced modes (red) were also shown in the figures.

In Figs. 31(a)–31(c), we display with dashed blue lines the frequency response  $G_c(i\omega)$  of the LQG closed-loop system when solving the full-order ( $n=220$ ) Riccati equations. Comparing the dashed blue lines in Fig. 22, where the frequency response of the reduced model of the open loop is shown, with the ones of the closed loop in Fig. 31, we see that the most unstable frequencies are reduced by an order of magnitude. Solving the Riccati equations for the reduced models of order  $r=2, 4$ , and  $6$  for the three sets of modes (global, POD, and balanced modes), we observe the same trend for the closed-loop system as we saw for the open-loop system: The reduced-order model based on two balanced modes (red line in Fig. 31(b)) is able to obtain a closed-loop performance very similar to the full model, whereas POD modes require a substantially larger basis and global modes fail entirely.

It should be mentioned that model reduction for unstable systems is also possible using global modes [10], POD modes [104], and, more recently, balanced modes [105].

## 6 Conclusion

A unifying framework for linear fluid dynamical systems has been presented and reviewed that allows the analysis of stability and response characteristics and the design of optimal and robust control schemes. An input-output formulation of the governing equations yields a flexible formulation for treating stability problems and for developing control strategies that optimize given objectives while still satisfying prescribed constraints.

The linear Ginzburg–Landau equation on the infinite domain has been used as a model equation to demonstrate the various concepts and tools. It has been modified to capture both subcritical and supercritical disturbance dynamics and thus span the range of fluid behavior observed in various generic shear flow configurations. With a small modification, the equation can also be used to mimic instabilities in other spatially developing flows, for instance, flows on semi-infinite domains such as inhomogeneous jets and wakes.

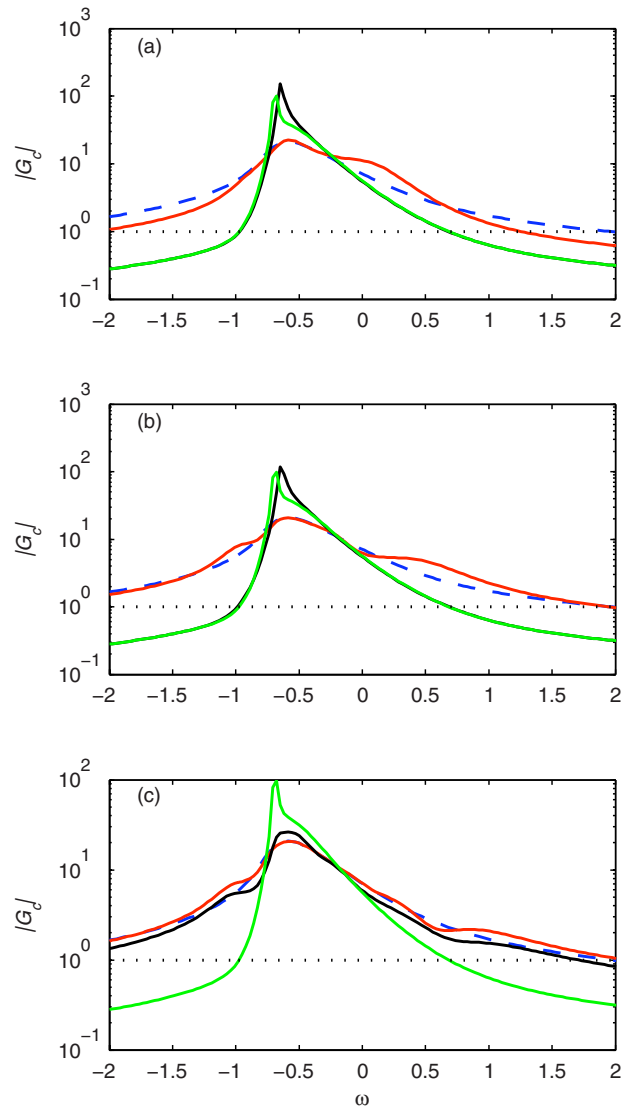


**Fig. 31 The frequency response of the closed feedback loop based on a LQG compensator.** The blue dashed lines represent the full model of order  $n=220$ . The performance of reduced-order models based on  $r=2, 4$ , and  $6$  modes are shown in (a), (b), and (c), respectively. The red lines represent the balanced modes, the black lines represent the POD modes, and the green lines represent the global eigenmodes. We observe that reduced-order controller based on balanced modes outperforms the other two models. The poor performance of the reduced order based on POD and global modes is directly associated with the unsatisfactory approximation of the open-loop case in Fig. 22.

Input-output-based analysis tools, such as the impulse response or the frequency response, have been applied to the model equation. This type of analysis lays the foundation for a thorough understanding of the disturbance behavior and the design of effective control strategies. Concepts such as controllability and observability play an important role for both the input-output behavior and the control design.

The design of effective and efficient control strategies is a challenging task, starting with the placement of actuators and sensors and ending with the judicious choice of a model reduction basis in order to numerically solve the compensator problem. Along the way, compromises between optimality ( $\mathcal{H}_2$ -control) and robustness ( $\mathcal{H}_\infty$ -control) have to be made that influence the overall performance of the feedback system.

It is hoped that this review has given a comprehensive and modern introduction to the fields of stability and control theory and has shown the close link between them. It is further hoped that it will spark interest in the fluid dynamics community to continue the exploration of these two exciting disciplines.

The MATLAB files to reproduce the results and figures of this review article are available from the FTP server.<sup>1</sup>

## Acknowledgment

This work was partially sponsored by the Air Force Office of Scientific Research, under Grant/Contract No. FA8655-07-1-3053 through the EOARD. The first author acknowledges financial support by École Polytechnique and the Swedish research council (VR) for his stay at LadHyX where part of this work was performed.

## Appendix: Discretization

The numerical studies in this review article are based on a pseudospectral discretization of the Ginzburg–Landau operator  $\mathcal{A}$  using Hermite functions and the corresponding differentiation matrices provided by Weideman and Reddy [106]. To approximate the derivatives in Eq. (1), we expand the solution  $q(x, t)$  in  $n$  Hermite functions

$$q(x, t) = \sum_{j=1}^n \alpha_j(t) \exp\left(-\frac{1}{2} b^2 x^2\right) H_{j-1}(bx) \quad (\text{A1})$$

where  $H_j(bx)$  refers to the  $j$ th Hermite polynomial. The differentiation process is exact for solutions of the form

$$f(x) = \exp\left(-\frac{1}{2} b^2 x^2\right) p(bx) \quad (\text{A2})$$

where  $p(bx)$  is any polynomial of degree  $n-1$  or less. The scaling parameter  $b$  can be used to optimize the accuracy of the spectral discretization [107]. A comparison of the above expression with the analytical form of the global Ginzburg–Landau eigenmodes (9b) shows that they are of the same form except for the exponential term  $\exp((\nu/2\gamma)x)$  stemming from the convective part of the Ginzburg–Landau equation. This exponential term is responsible for the nonorthogonality of the eigenmodes of  $\mathcal{A}$ . The Hermite functions are thus the “orthogonal part” of the global modes. By choosing the Hermite function scaling factor  $b=\chi$ , we obtain a highly accurate approximation of  $\mathcal{A}$ , since any solution of the Ginzburg–Landau equation will decay with the same exponential rate as the Hermite functions in the limit as the domain tends to infinity.

The collocation points  $x_1, \dots, x_n$  are given by the roots of  $H_n(bx)$ . We also notice that the boundary conditions are enforced implicitly and that  $-x_1 = x_n = \mathcal{O}(\sqrt{bn})$  in the limit as  $n \rightarrow \infty$  [108]. The discretization converts the operator  $\mathcal{A}$  into a matrix  $A$  of size  $n \times n$  (with  $n$  as the number of collocation points). Throughout this review article, we present the results for  $n=220$  yielding a computational domain with  $x \in [-85, 85]$ .

Discretization transforms flow variable  $q(x, t)$  into a column vector  $\hat{q}(t)$  of dimension  $n$ , and the inner product is defined as

$$\langle f, g \rangle = \int_{-\infty}^{\infty} f(x)^* g(x) dx \approx \sum_{i=1}^n \sum_{j=1}^n \hat{f}_i^H \hat{g}_j w_{i,j} = \hat{f}^H M \hat{g} = \langle \hat{f}, \hat{g} \rangle_M \quad (\text{A3})$$

where  $\hat{f} = [\hat{f}_1, \dots, \hat{f}_n]^H$  and  $\hat{g} = [\hat{g}_1, \dots, \hat{g}_n]^H$  are the column vectors consisting of, respectively,  $f(x)$  and  $g(x)$  evaluated at the collocation points. The symbol  $H$  denotes the Hermitian (complex conjugate transpose) operation. The positive-definite matrix  $M$  con-

tains the weights  $w_{i,j}$  of the chosen quadrature rule. For instance, applying the trapezoidal rule to the Hermite collocation points results in a diagonal matrix  $M = \frac{1}{2} \text{diag}\{\Delta x_1, \Delta x_2 + \Delta x_1, \dots, \Delta x_{n-1} + \Delta x_{n-2}, \Delta x_{n-1}\}$ , with  $\Delta x_i = x_{i+1} - x_i$ . In this paper, the discrete variables  $\hat{f}$  are denoted by  $f$ .

The operators  $B$  and  $C$ , describing the input and output configurations, are represented at their respective collocation points. We assume a spatial distribution of inputs  $B = \{B_1, \dots, B_p\}$  and outputs  $C = \{C_1, \dots, C_r\}^T$  in the form of Gaussian functions

$$B_i u(t) = \exp\left[-\left(\frac{x - x_{w,i}}{s}\right)^2\right] u(t) \quad (\text{A4a})$$

$$C_i q(t) = \exp\left[-\left(\frac{x - x_{s,i}}{s}\right)^2\right]^H M q(t) \quad (\text{A4b})$$

where  $x$  represents the Hermite collocation points.

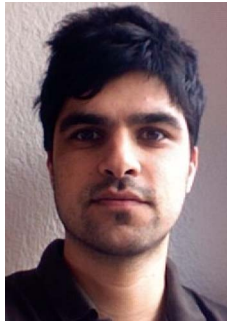
## References

- [1] Butler, K. M., and Farrell, B. F., 1992, “Three-Dimensional Optimal Perturbations in Viscous Shear Flow,” *Phys. Fluids A*, **4**, pp. 1637–1650.
- [2] Farrell, B. F., 1988, “Optimal Excitation of Perturbations in Viscous Shear Flow,” *Phys. Fluids*, **31**, pp. 2093–2102.
- [3] Reddy, S. C., and Henningson, D. S., 1993, “Energy Growth in Viscous Channel Flows,” *J. Fluid Mech.*, **252**, pp. 209–238.
- [4] Reddy, S. C., Schmid, P. J., and Henningson, D. S., 1993, “Pseudospectra of the Orr–Sommerfeld Operator,” *SIAM J. Appl. Math.*, **53**(1), pp. 15–47.
- [5] Farrell, B. F., and Ioannou, P. J., 1996, “Generalized Stability Theory. Part I. Autonomous Operators,” *J. Atmos. Sci.*, **53**, pp. 2025–2040.
- [6] Schmid, P. J., 2007, “Nonmodal Stability Theory,” *Annu. Rev. Fluid Mech.*, **39**, pp. 129–162.
- [7] Schmid, P. J., and Henningson, D. S., 2001, *Stability and Transition in Shear Flows*, Springer, New York.
- [8] Trefethen, L. N., Trefethen, A. E., Reddy, S. C., and Driscoll, T., 1993, “Hydrodynamic Stability Without Eigenvalues,” *Science*, **261**, pp. 578–584.
- [9] Jovanovic, M. R., and Bamieh, B., 2005, “Componentwise Energy Amplification in Channel Flows,” *J. Fluid Mech.*, **534**, pp. 145–183.
- [10] Åkervik, E., Hoepffner, J., Ehrenstein, U., and Henningson, D. S., 2007, “Optimal Growth, Model Reduction and Control in a Separated Boundary-Layer Flow Using Global Eigenmodes,” *J. Fluid Mech.*, **579**, pp. 305–314.
- [11] Bewley, T. R., and Liu, S., 1998, “Optimal and Robust Control and Estimation of Linear Paths to Transition,” *J. Fluid Mech.*, **365**, pp. 305–349.
- [12] Chevalier, M., Hoepffner, J., Åkervik, E., and Henningson, D. S., 2007, “Linear Feedback Control and Estimation Applied to Instabilities in Spatially Developing Boundary Layers,” *J. Fluid Mech.*, **588**, pp. 163–187.
- [13] Chevalier, M., Hoepffner, J., Bewley, T. R., and Henningson, D. S., 2006, “State Estimation in Wall-Bounded Flow Systems. Part 2: Turbulent Flows,” *J. Fluid Mech.*, **552**, pp. 167–187.
- [14] Hoepffner, J., Chevalier, M., Bewley, T. R., and Henningson, D. S., 2005, “State Estimation in Wall-Bounded Flow Systems. Part I: Laminar Flows,” *J. Fluid Mech.*, **534**, pp. 263–294.
- [15] Höglberg, M., Bewley, T. R., and Henningson, D. S., 2003, “Linear Feedback Control and Estimation of Transition in Plane Channel Flow,” *J. Fluid Mech.*, **481**, pp. 149–175.
- [16] Höglberg, M., Bewley, T. R., and Henningson, D. S., 2003, “Relaminarization of  $Re_c=100$  Turbulence Using Gain Scheduling and Linear State-Feedback Control Flow,” *Phys. Fluids*, **15**, pp. 3572–3575.
- [17] Joshi, S. S., Speyer, J. L., and Kim, J., 1997, “A Systems Theory Approach to the Feedback Stabilization of Infinitesimal and Finite-Amplitude Disturbances in Plane Poiseuille Flow,” *J. Fluid Mech.*, **332**, pp. 157–184.
- [18] Lee, K. H., Cortelezzi, L., Kim, J., and Speyer, J., 2001, “Application of Reduced-Order Controllers to Turbulent Flow for Drag Reduction,” *Phys. Fluids*, **13**, pp. 1321–1330.
- [19] Monokrousos, A., Brandt, L., Schlatter, P., and Henningson, D. S., 2008, “DNS and Least of Estimation and Control of Transition in Boundary Layers Subject to Free-Stream Turbulence,” *Int. J. Heat Fluid Flow*, **29**(3), pp. 841–855.
- [20] Anderson, B., and Moore, J., 1990, *Optimal Control: Linear Quadratic Methods*, Prentice-Hall, New York.
- [21] Kwakernaak, H., and Sivan, R., 1972, *Linear Optimal Control Systems*, Wiley Interscience, New York.
- [22] Lewis, F. L., and Syrmos, L. V., 1995, *Optimal Control*, Wiley, New York.
- [23] Zhou, K., Doyle, J. C., and Glover, K., 2002, *Robust and Optimal Control*, Prentice-Hall, Englewood Cliffs, NJ.
- [24] Bewley, T. R., 2001, “Flow Control: New challenges for a New Renaissance,” *Prog. Aerosp. Sci.*, **37**, pp. 21–58.
- [25] Gal-El-Hak, M., 1996, “Modern Developments in Flow Control,” *Appl. Mech. Rev.*, **49**, pp. 365–379.
- [26] Kim, J., 2003, “Control of Turbulent Boundary Layers,” *Phys. Fluids*, **15**, pp. 1093–1105.

<sup>1</sup><ftp://ftp.mech.kth.se/pub/review>.

- [27] Kim, J., and Bewley, T. R., 2007, "A Linear Systems Approach to Flow Control," *Annu. Rev. Fluid Mech.*, **39**, pp. 383–417.
- [28] Hill, D. C., 1995, "Adjoint Systems and Their Role in the Receptivity Problem for Boundary Layers," *J. Fluid Mech.*, **292**, pp. 183–204.
- [29] Luchini, P., and Bottaro, A., 1998, "Gortler Vortices: A Backward-in-Time Approach to the Receptivity Problem," *J. Fluid Mech.*, **363**, pp. 1–23.
- [30] Chomaz, J. M., 2005, "Global Instabilities in Spatially Developing Flows: Non-Normality and Nonlinearity," *Annu. Rev. Fluid Mech.*, **37**, pp. 357–392.
- [31] Huerre, P., and Monkewitz, P. A., 1990, "Local and Global Instabilities in Spatially Developing Flows," *Annu. Rev. Fluid Mech.*, **22**, pp. 473–573.
- [32] Cohen, K., Siegel, S., McLaughlin, T., Gillies, E., and Myatt, J., 2005, "Closed-Loop Approaches to Control of a Wake Flow Modeled by the Ginzburg-Landau Equation," *Comput. Fluids*, **34**, pp. 927–949.
- [33] Lauga, E., and Bewley, T. R., 2003, "The Decay of Stabilizability With Reynolds Number in a Linear Model of Spatially Developing Flows," *Proc. R. Soc. London, Ser. A*, **459**, pp. 2077–2095.
- [34] Lauga, E., and Bewley, T. R., 2004, "Performance of a Linear Robust Control Strategy on a Nonlinear Model of Spatially Developing Flows," *J. Fluid Mech.*, **512**, pp. 343–374.
- [35] Monkewitz, P., 1989, "Feedback Control of Global Oscillations in Fluid Systems," AIAA Paper No. 89-0991.
- [36] Park, D. S., Ladd, D. M., and Hendricks, E. W., 1993, "Feedback Control of a Global Mode in Spatially Developing Flows," *Phys. Lett. A*, **182**, pp. 244–248.
- [37] Briggs, R. J., 1964, *Electron-Stream Interaction With Plasmas*, MIT, Cambridge, MA.
- [38] Huerre, P., 2000, "Open Shear Flow Instabilities," *Perspectives in Fluid Dynamics*, Cambridge University Press, Cambridge, England, pp. 159–229.
- [39] Chomaz, J. M., Huerre, P., and Redekopp, L. G., 1991, "A Frequency Selection Criterion in Spatially Developing Flows," *Stud. Appl. Math.*, **84**, pp. 119–144.
- [40] Le Dizes, S., Huerre, P., Chomaz, J. M., and Monkewitz, P. A., 1996, "Linear Global Modes in Spatially Developing Media," *Philos. Trans. R. Soc. London, Ser. A*, **354**, pp. 169–212.
- [41] Monkewitz, P., 1990, "The Role of Absolute and Convective Instability in Predicting the Behavior of Fluid Systems," *Eur. J. Mech. B/Fluids*, **9**, pp. 395–413.
- [42] Davies, E. B., 2002, "Non-Self-Adjoint Differential Operators," *Bull. London Math. Soc.*, **34**, pp. 513–532.
- [43] Trefethen, L. N., 1997, "Pseudospectra of Linear Operators," *SIAM Rev.*, **39**(3), pp. 383–406.
- [44] Trefethen, L. N., and Embree, M., 2005, *Spectra and Pseudospectra: The Behavior of Nonnormal Matrices and Operators*, Princeton University Press, Princeton, NJ.
- [45] Chomaz, J. M., Huerre, P., and Redekopp, L. G., 1991, "The Effect of Nonlinearity and Forcing on Global Modes," *New Trends in Nonlinear Dynamics and Pattern-Forming Phenomena* (NATO Advanced Series Institute, Series B: Physics), P. Coullet and P. Huerre, eds., Springer, New York, pp. 259–274.
- [46] Cossu, C., and Chomaz, J. M., 1997, "Global Measures of Local Convective Instabilities," *Phys. Rev. Lett.*, **78**, pp. 4387–4390.
- [47] Henningson, D. S., and Åkervik, E., 2008, "The Use of Global Modes to Understand Transition and Perform Flow Control," *Phys. Fluids*, **20**, p. 031302.
- [48] Hunt, R. E., and Crighton, D. G., 1991, "Instability of Flows in Spatially Developing Media," *Proc. R. Soc. London, Ser. A*, **435**, pp. 109–128.
- [49] Chomaz, J. M., Huerre, P., and Redekopp, L. G., 1988, "Bifurcations to Local and Global Modes in Spatially Developing Flows," *Phys. Rev. Lett.*, **60**, pp. 25–28.
- [50] Chomaz, J. M., Huerre, P., and Redekopp, L. G., 1987, "Models of Hydrodynamic Resonances in Separated Shear Flows," Sixth Symposium on Turbulent Shear Flows, Toulouse, France.
- [51] Åkervik, E., Ehrenstein, U., Gallaire, F., and Henningson, D. S., 2008, "Global Two-Dimensional Stability Measures of the Flat Plate Boundary-Layer Flow," *Eur. J. Mech. B/Fluids*, **27**, pp. 501–513.
- [52] Ehrenstein, U., and Gallaire, F., 2005, "On Two-Dimensional Temporal Modes in Spatially Evolving Open Flows: The Flat-Plate Boundary Layer," *J. Fluid Mech.*, **536**, pp. 209–218.
- [53] Trefethen, L. N., and Bau, D., 1997, *Numerical Linear Algebra*, SIAM, Philadelphia.
- [54] Andersson, P., Berggren, M., and Henningson, D. S., 1999, "Optimal Disturbances and Bypass Transition in Boundary Layers," *Phys. Fluids*, **11**, pp. 134–150.
- [55] Corbett, P., and Bottaro, A., 2001, "Optimal Linear Growth in Swept Boundary Layers," *J. Fluid Mech.*, **435**, pp. 1–23.
- [56] Luchini, P., 2000, "Reynolds-Number-Independent Instability of the Boundary Layer Over a Flat Surface: Optimal Perturbations," *J. Fluid Mech.*, **404**, pp. 289–309.
- [57] Biau, D., and Bottaro, A., 2004, "Transient Growth and Minimal Defects: Two Possible Initial Paths of Transition to Turbulence in Plane Shear Flows," *Phys. Fluids*, **16**, pp. 3515–3529.
- [58] Giannetti, F., and Luchini, P., 2007, "Structural Sensitivity of the First Instability of the Cylinder Wake," *J. Fluid Mech.*, **581**, pp. 167–197.
- [59] Pier, B., 2002, "On the Frequency Selection of Finite-Amplitude Vortex Sheding in the Cylinder Wake," *J. Fluid Mech.*, **458**, pp. 407–417.
- [60] Provansal, M., Mathis, C., and Boyer, L., 1987, "Bénard-von Kármán Instability: Transient and Forcing Regimes," *J. Fluid Mech.*, **182**, pp. 1–22.
- [61] Albarède, P., and Monkewitz, P. A., 1992, "A Model for the Formation of Oblique Shedding and "Chevron" Patterns in Cylinder Wakes," *Phys. Fluids A*, **4**, pp. 744–756.
- [62] Monkewitz, P. A., Williamson, C. H. K., and Miller, G. D., 1996, "Phase Dynamics of Kármán Vortices in Cylinder Wakes," *Phys. Fluids*, **8**, pp. 91–96.
- [63] Roussopoulos, K., and Monkewitz, P., 1996, "Nonlinear Modeling of Vortex Sheding Control in Cylinder Wakes," *Physica D*, **97**, pp. 264–273.
- [64] Lesshaft, L., Huerre, P., Sagaut, P., and Terracol, M., 2006, "Nonlinear Global Modes in Hot Jets," *J. Fluid Mech.*, **554**, pp. 393–409.
- [65] Nichols, J. W., Schmid, P. J., and Riley, J. J., 2007, "Self-Sustained Oscillations in Variable-Density Round Jets," *J. Fluid Mech.*, **582**, pp. 341–376.
- [66] Marquillie, M., and Ehrenstein, U., 2002, "On the Onset of Nonlinear Oscillations in a Separating Boundary-Layer Flow," *J. Fluid Mech.*, **458**, pp. 407–417.
- [67] Ho, C. M., and Huerre, P., 1984, "Perturbed Free Shear Layers," *Annu. Rev. Fluid Mech.*, **16**, pp. 365–424.
- [68] Kailath, T., 1980, *Linear Systems*, Prentice-Hall, Englewood Cliffs, NJ.
- [69] Farrell, B. F., and Ioannou, P. J., 1993, "Stochastic Forcing of the Linearized Navier-Stokes Equations," *Phys. Fluids A*, **5**, pp. 2600–2609.
- [70] van der Schaft, A. J., 1991, "Duality for Linear Systems: External and State Space Characterization of the Adjoint Problem," *Analysis of Controlled Dynamical Systems*, B. Bonnard B. Bride, J. P. Gauthier, and I. Kupka, eds., Birkhäuser, Boston, pp. 393–403.
- [71] Hoepffner, J., 2006, "Stability and Control of Shear Flows Subject to Stochastic Excitations," Ph.D. thesis, KTH Stockholm, Stockholm.
- [72] Bamieh, B., and Dahleh, M., 2001, "Energy Amplification in Channel Flows With Stochastic Excitation," *Phys. Fluids*, **13**, pp. 3258–3269.
- [73] Hoepffner, J., and Brandt, L., 2008, "Stochastic Approach to the Receptivity Problem Applied to Bypass Transition in Boundary Layers," *Phys. Fluids*, **20**, pp. 024108.
- [74] Datta, B., 2003, *Numerical Methods for Linear Control Systems Design and Analysis*, Elsevier, New York.
- [75] Zhou, K., Salomon, G., and Wu, E., 1999, "Balanced Realization and Model Reduction for Unstable Systems," *Int. J. Robust Nonlinear Control*, **9**, pp. 183–198.
- [76] Antoulas, C. A., 2005, *Approximation of Large-Scale Dynamical Systems*, SIAM, Philadelphia.
- [77] Lumley, J. L., 1970, *Stochastic Tools in Turbulence*, Academic, New York.
- [78] Obinata, G., and Andersson, B. D., 2001, *Model Reduction for Control System Design*, Springer, New York.
- [79] Green, M., and Limebeer, J. N., 1995, *Linear Robust Control*, Prentice-Hall, Englewood Cliffs, NJ.
- [80] Skogestad, S., and Postlethwaite, I., 2005, *Multivariable Feedback Control: Analysis and Design*, 2nd ed., Wiley, New York.
- [81] Moore, B., 1981, "Principal Component Analysis in Linear Systems: Controllability, Observability, and Model Reduction," *IEEE Trans. Autom. Control*, **26**(1), pp. 17–32.
- [82] Antoulas, A. C., Sorensen, D. S., and Gugercin, S., 2001, "A Survey of Model Reduction Methods for Large-Scale Systems," *Contemp. Math.*, **280**, pp. 193–219.
- [83] C. W. Rowley, 2005, "Model Reduction for Fluids Using Balanced Proper Orthogonal Decomposition," *Int. J. Bifurcation Chaos Appl. Sci. Eng.*, **15**(3), pp. 997–1013.
- [84] Willcox, K., and Peraire, J., 2002, "Balanced Model Reduction Via the Proper Orthogonal Decomposition," *AIAA J.*, **40**(11), pp. 2323–2330.
- [85] Sirovich, L., 1987, "Turbulence and the Dynamics of Coherent Structures. Parts I–III," *Q. Appl. Math.*, **45**, pp. 561–590.
- [86] Ilak, M., and Rowley, C. W., 2008, "Modeling of Transitional Channel Flow Using Balanced Proper Orthogonal Decomposition," *Phys. Fluids*, **20**, p. 034103.
- [87] Ahuja, S., Rowley, C. W., Kevrekidis, I. G., and Wei, M., 2007, "Low-Dimensional Models for Control of Leading-Edge Vortices: Equilibria and Linearized Models," 45th AIAA Aerospace Sciences Meeting and Exhibit, AIAA Paper No. 2007-709.
- [88] Joslin, R. D., 1998, "Aircraft Laminar Flow Control," *Annu. Rev. Fluid Mech.*, **30**, pp. 1–29.
- [89] Moin, P., and Bewley, T. R., 1994, "Feedback Control of Turbulence," *Appl. Mech. Rev.*, **47**(6), pp. S3–S113.
- [90] Choi, H., Moin, P., and Kim, J., 1994, "Active Turbulence Control for Drag Reduction in Wall-Bounded Flows," *J. Fluid Mech.*, **262**, pp. 75–110.
- [91] Bewley, T. R., and Moin, P., 1994, "Optimal Control of Turbulent Channel Flows," *Active Control of Vibration and Noise*, ASME DE-Vol. No. 75, E. W. Hendricks, K. W. Wang, A. H. Von Flotow, R. Shoureshi, and T. W. Farabee, eds., ASME, New York, NY.
- [92] Bewley, T. R., Moin, P., and Temam, R., 2001, "DNS-Based Predictive Control of Turbulence: An Optimal Benchmark for Feedback Algorithms," *J. Fluid Mech.*, **447**, pp. 179–225.
- [93] Guégan, A., Schmid, P. J., and Huerre, P., 2006, "Optimal Energy Growth and Optimal Control in Swept Hiemenz Flow," *J. Fluid Mech.*, **566**, pp. 11–45.
- [94] Zuccher, P., Luchini, S., and Bottaro, A., 2006, "Algebraic Growth in a Blasius Boundary Layer: Optimal and Robust Control by Mean Suction in the Nonlinear Regime," *J. Fluid Mech.*, **556**, pp. 189–216.
- [95] Farrell, B. F., and Ioannou, P. J., 2000, *Flow Control: Passive, Active and Reactive Flow Management*, Cambridge University Press, London.
- [96] Gunzburger, M. D., 1995, *Flow Control*, Springer, Berlin.
- [97] Skelton, R., Iwasaki, T., and Grigoriadis, K., 1998, *A Unified Algebraic Approach to Linear Control Design*, Taylor & Francis, London.
- [98] Kalman, R. E., 1960, "A New Approach to Linear Filtering and Prediction Problems," *Trans. ASME Ser. D. J. Basic Eng.*, **82**, pp. 24–45.

- [99] Laub, A. J., 1991, "Invariant Subspace Methods for the Numerical Solution of Riccati Equations," *The Riccati Equation*, S. Bittanti, A. J. Laub, and J. C. Willems, eds., Springer, Berlin, pp. 163–196.
- [100] Höglberg, M., 2001, "Optimal Control of Boundary-Layer Transition," Ph.D. thesis, KTH Stockholm, Stockholm.
- [101] Doyle, J., 1978, "Guaranteed Margins for LQG Regulators," *IEEE Trans. Autom. Control*, **23**, pp. 756–757.
- [102] Doyle, J. C., Glover, K., Khargonekar, P. P., and Francis, B. A., 1989, "State-Space Solutions to Standard  $H_2$  and  $H^\infty$  Control Problems," *IEEE Trans. Autom. Control*, **34**, pp. 831–847.
- [103] Kailath, T., 1973, "Some New Algorithms for Recursive Estimation in Constant Linear Systems," *IEEE Trans. Inf. Theory*, **19**, pp. 750–760.
- [104] Gillies, E. A., 1998, "Low-Dimensional Control of the Circular Cylinder Wake," *J. Fluid Mech.*, **371**, pp. 157–178.
- [105] Ahuja, S., and Rowley, C. W., 2008, "Low-Dimensional Models for Feed-back Stabilization of Unstable Steady States," 46th AIAA Aerospace Sciences Meeting and Exhibit, AIAA Paper No. 2008-553.
- [106] Weideman, J. A. C., and Reddy, S. C., 2000, "A MATLAB Differentiation Matrix Suite," *ACM Trans. Math. Softw.*, **26**, pp. 465–519.
- [107] Tang, T., 1993, "The Hermite Spectral Method for Gaussian-Type Functions," *J. Sci. Comput.*, **14**, pp. 594–606.
- [108] Abramowitz, M., and Stegun, I. E., 1964, *Handbook of Mathematical Functions: With Formulas, Graphs, and Mathematical Tables*, National Bureau of Standards, Washington, DC.



**Shervin Bagheri** is a Ph.D. student at the Department of Mechanics at KTH in Stockholm. He completed his undergraduate studies in Physics Engineering and Scientific Computing at Uppsala University in Sweden in 2006. His Ph.D. project involves mainly model reduction and control of spatially developing flows.



**Jérôme Hœppner** was born in France in 1978. After completing his undergraduate studies at Université Paul Sabatier in Toulouse/France, he went to the Royal Institute of Technology (KTH) in Stockholm, Sweden to do his Ph.D. thesis, which he defended in 2006. His research interests focus on the study of hydrodynamic instabilities and their control.



**Peter Schmid** received a Ph.D. in Mathematics from the Massachusetts Institute of Technology (Cambridge, MA) in 1993. He has been an Assistant Professor, an Associate Professor, and a Full Professor at the Department of Applied Mathematics of the University of Washington in Seattle, WA. He is now a Research Director with the French Centre National de la Recherche Scientifique (CNRS) at the Laboratoire d'Hydrodynamique (LadHyX) and a Professeur (chargé de cours) of Mechanics at the École Polytechnique in Palaiseau near Paris. His research is in the area of hydrodynamic stability theory, flow control, and computational fluid dynamics.



**Dan Henningson** is a Professor at the Department of Mechanics at KTH in Stockholm. He received his PhD in the same department 1988, after which he joined the Department of Mathematics at MIT as an assistant professor. Four years later, 1992, he came back to Sweden to become an Adjunct Professor at the Department of Mechanics, KTH and a Senior Research Scientist at FFA (The Aeronautical Research Institute of Sweden). In 1999, he became a Full Professor at the Department of Mechanics, which he now also heads. In addition, he is the Director of the Linné Flow Center; a center of excellence in fundamental fluid mechanics supported by the Swedish Research Council. He is also an Associate Editor of the *Journal of Fluid Mechanics*. His research areas include stability of fluid flows, transition to turbulence, and both feedback and optimal control of fluid flows. The research is mainly computational and often involves large scale supercomputing. Dr. Henningson authored or co-authored well over 100 papers and several books, among them the monograph *Stability and Transition in Shear Flow*, published by Springer in 2001.